ARTICLES
https://doi.org/10.1038/s41563-020-0755-z

nature materials

The dose threshold for nanoparticle tumour delivery

Ben Ouyang[1,2,3], Wilson Poon[2,3,12], Yi-Nan Zhang[2,3,12], Zachary P. Lin[2,3], Benjamin R. Kingston[2,3], Anthony J. Tavares[2,3,4], Yuwei Zhang[3,5], Juan Chen[6], Michael S. Valic[6], Abdullah M. Syed[2,3,7], Presley MacMillan[3,5], Julien Couture-Senécal[2,3,8], Gang Zheng[2,6,9] and Warren C. W. Chan[2,3,5,10,11] ✉

Nanoparticle delivery to solid tumours over the past ten years has stagnated at a median of 0.7% of the injected dose. Varying nanoparticle designs and strategies have yielded only minor improvements. Here we discovered a dose threshold for improving nanoparticle tumour delivery: 1 trillion nanoparticles in mice. Doses above this threshold overwhelmed Kupffer cell uptake rates, nonlinearly decreased liver clearance, prolonged circulation and increased nanoparticle tumour delivery. This enabled up to 12% tumour delivery efficiency and delivery to 93% of cells in tumours, and also improved the therapeutic efficacy of Caelyx/Doxil. This threshold was robust across different nanoparticle types, tumour models and studies across ten years of the literature. Our results have implications for human translation and highlight a simple, but powerful, principle for designing nanoparticle cancer treatments.

The delivery of nanoparticles into solid tumours is critical to their utility for diagnosing and treating cancer. We recently showed that 0.7% (median) of nanoparticles are successfully delivered to solid tumours, and this low value has contributed to the poor clinical translation of nanomedicines[1]. The results of that study inspired many researchers to explore different avenues to increase the efficiency of nanoparticle delivery. These included changing physicochemical properties of nanoparticles such as size[2,3], shape[4,5] and surface chemistry[6,7], or using biological techniques such as ablating[8,9] or saturating Kupffer cells[10]. Although there have been minor increases[11], the challenge is that none of these approaches present a central and systematic principle for improving delivery efficiency. Given that delivery has become a major problem in nanotechnology and many emerging technologies such as genome editing and immunotherapy, there is a need to develop universal principles of improving the delivery efficiency of nanoparticles to the target site. These principles could be developed by re-evaluating previous fundamental studies or designing strategies to overcome the barriers that block nanoparticle delivery to tumours. Solving this delivery problem is essential to the translation and utility of nanotechnology for treating cancer and other diseases.

Here we addressed this delivery problem by discovering a dose threshold that has to be breached to enable predictable and significant delivery. This threshold exists at the kinetic limits of nanoparticle uptake by Kupffer cells and not their total capacity. Our results present an important dose threshold principle for nanoparticle delivery with potential implications that could inform human clinical translation.

The dose threshold for liver clearance

We began the study by evaluating the relationship between nanoparticle dose and liver clearance. The liver is the largest reticuloendothelial system (RES) organ and it takes up a significant portion of administered nanoparticles[12]. We hypothesized that the proportional nanoparticle uptake by the liver would decrease significantly once the dose surpassed maximum Kupffer cell uptake rates. This Kupffer cell interaction with nanoparticles at different doses is not well characterized and understood[10,13–16], despite studies that have reported contrasting pharmacokinetics at extreme doses[17–20]. We aimed to find a threshold dose that would begin to reduce liver clearance.

We injected 4T1 tumour-bearing BALB/c mice intravenously with varying numbers of 50 nm polyethylene glycol-conjugated (PEGylated) gold nanoparticles (Supplementary Fig. 1) that spanned 1,000-fold from 50 billion to 50 trillion nanoparticles. We chose gold nanoparticles because they are inert and can be detected over a broad range of doses with high sensitivity. We used tumour-bearing mice because the presence of tumours alters clearance of nanoparticles[21]. We euthanized the mice 24 h after injection and quantified gold biodistribution in tissues using inductively coupled plasma-mass spectrometry (ICP-MS). We observed that the liver accumulated a decreased proportion of injected nanoparticles as the dose increased (Fig. 1a). This corresponded to an increase in the nanoparticle blood half-life from 2 min to 8 h (Fig. 1b,c). This showed that liver clearance efficiency of PEGylated nanoparticles was limited at high doses.

We searched for a potential dose threshold. We investigated the number of nanoparticles that liver cells could take up over 24 h, a

[1]MD/PhD Program, University of Toronto, Toronto, Ontario, Canada. [2]Institute of Biomedical Engineering, University of Toronto, Toronto, Ontario, Canada. [3]Terrence Donnelly Centre for Cellular and Biomolecular Research, University of Toronto, Toronto, Ontario, Canada. [4]School of Life Sciences, Faculty of Humanities and Social Sciences, Sheridan College, Brampton, Ontario, Canada. [5]Department of Chemistry, University of Toronto, Toronto, Ontario, Canada. [6]Princess Margaret Cancer Centre, University Health Network, Toronto, Ontario, Canada. [7]J. David Gladstone Institutes, San Francisco, CA, USA. [8]Division of Engineering Science, University of Toronto, Toronto, Ontario, Canada. [9]Department of Medical Biophysics, University of Toronto, Toronto, Ontario, Canada. [10]Department of Chemical Engineering and Applied Chemistry, University of Toronto, Toronto, Ontario, Canada. [11]Department of Material Science and Engineering, University of Toronto, Toronto, Ontario, Canada. [12]These authors contributed equally: Wilson Poon, Yi-Nan Zhang.
✉e-mail: warren.chan@utoronto.ca

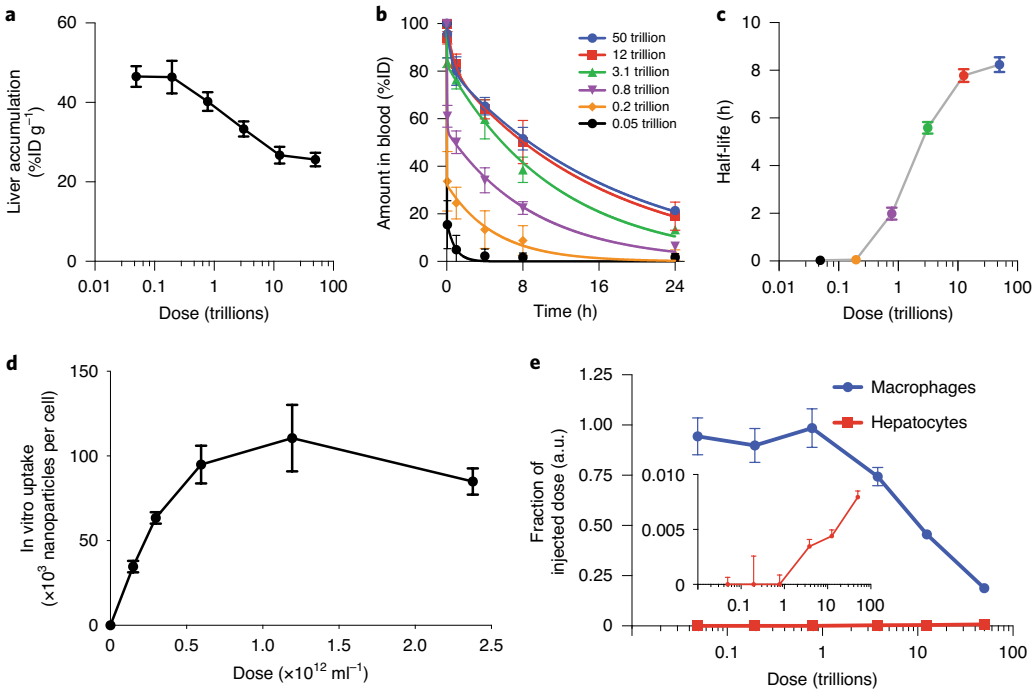

Fig. 1 | The liver clearance threshold. a, Liver accumulation of PEGylated gold nanoparticles 24 h post-injection as a function of dose, determined using ICP-MS. $n = 6$ mice. **b**, Nanoparticle blood kinetics as a function of dose. $n = 3$ mice. **c**, Half-life of nanoparticles as a function of dose. The legend in **b** also applies to **c**. $n = 3$ mice. **d**, In vitro macrophage uptake over 24 h as a function of dose. Uptake stopped increasing at approximately 100,000 nanoparticles per cell per 24-h period. $n = 3$ wells of cells. **e**, Quantification of the nanoparticle signal in liver F4/80$^+$ Kupffer cell macrophages and autofluorescent$^+$ hepatocytes using histology. Kupffer cell uptake reduced after a dose of 1 trillion nanoparticles, then hepatocytes (inset) took up nanoparticles. $n = 60$ cells from liver histology of 3 mice. All data points and error bars represent mean ± s.e.m. a.u. is arbitrary units.

commonly studied time point in nanoparticle research. Liver macrophage cells internalize the highest amount of nanoparticles, so we hypothesized that these macrophages were being overwhelmed. First, we incubated a macrophage cell line in vitro with different doses of gold nanoparticles. These cells accumulated approximately 100,000 nanoparticles per cell in 24 h (Fig. 1d). In vivo, mice have on the order of 10 million Kupffer cells[22,23], so we estimated that the total clearance rate limit of all Kupffer cells in a mouse liver was on the order of 1 trillion nanoparticles in 24 h. We analysed livers 24 h after nanoparticle administration using histology. We observed that Kupffer cells took up disproportionately fewer nanoparticles as the dose increased past a threshold single dose of 1 trillion nanoparticles (Fig. 1e and Supplementary Fig. 2). At doses above the threshold, a minor proportion of nanoparticles accumulated in hepatocytes (Fig. 1e and Supplementary Fig. 3), suggesting that hepatocytes served as a liver accumulation reservoir once Kupffer cells were overwhelmed, as previously reported[24,25]. We determined that this threshold was not due to Kupffer cell death as we did not observe liver cytotoxicity in the range of doses studied (Supplementary Figs. 4–6) and that this threshold was unrelated to the opsonin-mediated accelerated blood clearance (ABC) phenomenon[26] (Supplementary Fig. 7). Our results demonstrated that Kupffer cell uptake was fundamentally limited at single doses beyond 1 trillion nanoparticles in 24 h.

Mechanism of the dose threshold in Kupffer cells

We did not observe the total uptake capacity of Kupffer cells reaching saturation (Supplementary Fig. 8), so we hypothesized that high doses were instead overwhelming uptake rates. We used intravital microscopy to measure real-time nanoparticle uptake rates of in vivo Kupffer cells in the first 30 min after injection. We used Csf1r-EGFP mice[27] to identify Kupffer cells as cells expressing green fluorescent protein (GFP$^+$). We compared the Kupffer cell uptake rates of mice receiving a below-threshold low dose with mice receiving an above-threshold high dose. The low-dose mice received 0.2 trillion Cy3-labelled nanoparticles only (Fig. 2a and Supplementary Video 1). The high-dose mice received 0.2 trillion Cy3-labelled nanoparticles supplemented with 12 trillion Cy5-labelled nanoparticles (Fig. 2b and Supplementary Video 2). The nanoparticles were labelled with different dyes as markers for uptake rate (Cy3) versus uptake capacity (Cy5). Imaging in the Cy3 channel revealed that the absolute uptake of Cy3 nanoparticles in Kupffer cells was slower in mice that received a high dose than in mice that received a low dose (Fig. 2c,d). The higher doses inhibited uptake rates as more particles competed for uptake. We concurrently imaged these same cells in the Cy5 channel and observed them to continue to take up Cy5 nanoparticles (Fig. 2b,e and Supplementary Video 3). Transmission electron microscopy (TEM) showed that nanoparticles occupied a relatively minor volume in Kupffer cells at this time point (Supplementary Fig. 9). These images conclusively showed that macrophage uptake capacity was not saturated. This is in direct contrast to studies employing the RES blockade, which assume that capacity must be saturated by a pre-injection dose to reduce clearance of a second dose of therapeutic nanoparticles[10,13,14]. These results proved that large numbers of nanoparticles above the threshold overwhelmed liver clearance by overwhelming Kupffer cell uptake rates and not uptake capacities.

We next investigated three general pathways of uptake in Kupffer cells to understand why the uptake rates were overwhelmed at doses beyond a threshold: clathrin- and caveolin-mediated endocytosis, macropinocytosis and receptor-mediated phagocytosis. We ruled out caveolae or clathrin-mediated endocytosis processes because these form small vesicles that do not typically take up particles larger than 35 nm in Kupffer cells[28], and we did not observe single nanoparticles (95 nm hydrodynamic diameter) enveloped in such

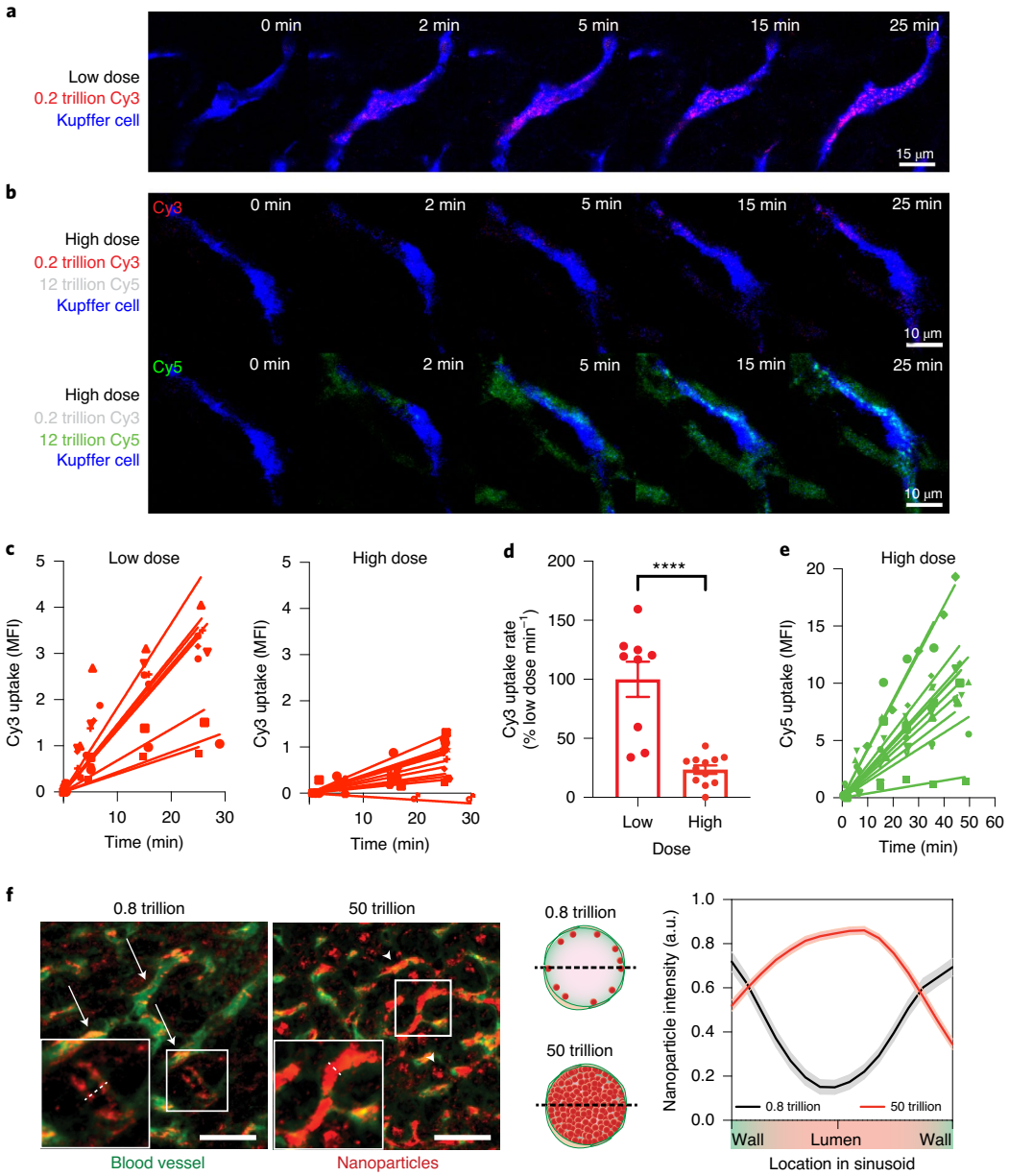

Fig. 2 | The dose threshold is determined by uptake rate. a, Live intravital imaging of Csf1r-EGFP mice livers. Mice were injected with 0.2 trillion Cy3-gold nanoparticles (red). Single EGFP$^+$ Kupffer cells (blue) were imaged over 25 min to determine gold nanoparticle uptake. **b**, Intravital imaging of Csf1r-EGFP mice livers. Mice were co-injected with 0.2 trillion Cy3-gold nanoparticles (red) and 12 trillion Cy5-gold nanoparticles (green). Top, imaging in the Cy3 channel. Bottom, imaging in the Cy5 channel. **c**, Total uptake of Cy3-labelled nanoparticles over 25 min from time-lapse sequences in **a** and **b**. Symbols represent individual Kupffer cells. Left, low dose ($n=9$ Kupffer cells from 3 mice). Right, high dose ($n=12$ Kupffer cells from 3 mice). **d**, Quantification of uptake rates over 25 min using the slopes in **c**. **e**, Total uptake of Cy5-labelled nanoparticles over 60 min in the same Kupffer cells in **b**. **f**, Left: imaging of liver CD209b$^+$ sinusoids (green) and dark-field$^+$ nanoparticles (red) 15 min after injection. Inset: ×2 magnification. Middle, right: nanoparticle quantification showed that nanoparticles distributed along walls for below-threshold (0.8 trillion) and in the lumen for above-threshold (50 trillion) doses. Scale bar, 40 μm. Lines with shaded envelopes represent mean ± s.e.m. $n=60$ blood vessel cross-sections from 3 mice. All data points and error bars represent mean ± s.e.m. Statistical significance was evaluated using a two-tailed unpaired Student's *t*-test. ****$P<0.0001$. Exact *P* values for **d**: $P=3.9\times10^{-5}$. MFI, mean fluorescence intensity.

endosomes on TEM images (Supplementary Fig. 10). We also ruled out dose-independent macropinocytosis because Cy3-labelled gold nanoparticles had poor intracellular localization with Cy5-labelled 70 kDa dextran, an established marker of macropinocytosis[29,30] (Supplementary Fig. 11). We instead hypothesized that Kupffer cells were taking up nanoparticles via receptor-mediated phagocytosis. TEM imaging of Kupffer cells 30 min after injection revealed that nanoparticles lined endosome membranes but were absent from their luminal centres (Supplementary Fig. 10), suggesting that only membrane-bound nanoparticles were internalized. Nanoparticles crowded most of the endosome membrane perimeters. This suggested that most of the available binding sites had been occupied and that higher doses could not bind for internalization. These patterns supported receptor-mediated phagocytosis. As protein coronas influence nanoparticle uptake[31], the adsorbed proteins on nanoparticles probably bound to Kupffer cell receptors. Further investigations

using dark-field histology 15 min after injection revealed that the lower dose of nanoparticles sparsely outlined sinusoidal walls, whereas the higher dose distributed centrally into the lumen (Fig. 2f). This further showed that higher doses overwhelmed receptors and binding sites on the walls of sinusoids. As contact between a nanoparticle and a Kupffer cell or liver sinusoidal endothelial cell is necessary to clear the nanoparticle from circulation[32], the excess unbound nanoparticles in the centre of the lumen had a lower probability of interacting with cells and therefore had a higher probability of exiting the sinusoid to continue circulating. We conclude that the nanoparticle dose threshold was correlated with the number of available receptors and binding sites on Kupffer cells. The specific receptors involved remain to be determined and should be identified in future work. Doses beyond this available binding site threshold overwhelmed the uptake rates of Kupffer cells, reduced liver clearance and prolonged circulation.

Modelling nanoparticle threshold uptake kinetics

Next we investigated how doses above the trillion threshold would affect delivery to the tumour. We created an in silico compartment model to characterize pharmacokinetics of nanoparticle transport from the blood to the liver and tumour (Supplementary Fig. 12a and Supplementary Methods). We limited the rate of uptake in the liver to 1 trillion nanoparticles in 24 h. We used two input doses: one below the threshold (0.2 trillion) and one above (50 trillion), and the model output included nanoparticle uptake rates in the liver and tumour. Our simulation showed that for the low dose, the uptake rate of the liver was always faster than that of the tumour (Supplementary Fig. 12b). For the high dose, the liver's uptake rate was proportionally lower than in the low-dose condition (Supplementary Fig. 12c). Mathematically integrating these uptake rates over the 24 h of circulation yielded the total accumulation over time. This showed that the high dose accumulated less in the liver and delivered more to the tumour (Supplementary Fig. 12d,e). We experimentally validated our compartment model using 4T1 tumour-bearing BALB/c mice injected with 0.2 or 50 trillion nanoparticles, and saw that the experimental results at 2, 8 and 24 h post-injection aligned with the modelling results (Supplementary Fig. 12d,e). This model was also adaptable to organic nanoparticles after adding a degradation term and tuning the affinity constants (Supplementary Fig. 13). These results suggested that administering more than 1 trillion nanoparticles overwhelmed liver uptake rates and led to greater tumour delivery.

Tumour delivery above the threshold dose

We investigated tumour delivery as a function of nanoparticle number to evaluate the dose threshold and characterize delivery beyond such a threshold. We injected 4T1 tumour-bearing BALB/c mice with gold nanoparticles of various sizes (Supplementary Fig. 1), spanning doses from 30 billion to 550 trillion (3×10^{10} to 5.5×10^{14}) nanoparticles. We confirmed experimentally in vivo that as the number of nanoparticles increased, tumour delivery increased (Fig. 3a) and liver accumulation decreased correspondingly (Fig. 3b). Around 1 trillion nanoparticles marked the inflection points of the beginning of this nonlinear dose dependence for both organs. This supports our results and theory that there is a minimal threshold dose that would begin to overwhelm the liver's clearance capacity and increase tumour delivery. We also compared the biodistribution of a single dose above this threshold against the same dose divided into multiple smaller doses below this threshold to test whether this effect was cumulative. This was not the case, because although the total number of nanoparticles was the same in both groups, the large single dose showed reduced liver accumulation, increased circulation half-life and increased tumour delivery (Supplementary Fig. 14). This was consistent with the principle that high numbers of nanoparticles overwhelmed liver uptake rates and not absolute uptake capacity. Together, these results confirmed that a single injection exceeding a threshold of 1 trillion nanoparticles improved tumour delivery.

Beyond 1 trillion nanoparticles, tumour delivery continued to increase. At the highest dose, the liver and tumour accumulated the same amount of nanoparticles, gram for gram. Tumour delivery efficiency was 0.03% of the injected dose at the lowest dose and 12% at the highest dose. This corresponded to a 7,300,000 times increase in absolute nanoparticle accumulation for only an 18,000 times increase in the number of nanoparticles injected. In contrast, the absolute accumulation in the liver increased only 6,000 times for the same increase in nanoparticle numbers. Notably, 12% in the tumour was more than an order of magnitude greater than the median 0.7% in the literature[1]. We observed that this increase in tumour delivery beyond this threshold was generally true for different mouse tumour models (xenogeneic, orthotopic and transgenetic, Fig. 3c–l) and nanoparticle compositions (silica and liposome, Fig. 3k,l and Supplementary Figs. 15 and 16). Nanoparticle accumulation in other organs, including the spleen, displayed no or minimal dose dependency, suggesting that this result was unique to the liver and tumour at this magnitude (Supplementary Fig. 17).

We were surprised to discover this threshold value only now, given the significant amount of studies on nanoparticle tumour delivery. This may be due to how dose is reported. In typical nanoparticle size-dependency studies, the doses are normalized to surface area or mass, which results in higher numbers of smaller nanoparticles. When we normalized the dose by units of surface area or mass, the threshold became obscured, the correlation of dose to tumour delivery dropped significantly and size-dependent accumulation in the tumour and liver emerged (Supplementary Fig. 18). This suggested that nanoparticle dose may be a confounding variable in size-dependency studies and it is hidden by the choice of normalization metric. Our data suggest that dose by number of nanoparticles may be a more appropriate descriptor than nanoparticle size. Biologically, the number of nanoparticles is more relevant

Fig. 3 | The dose threshold for tumour delivery. a, Tumour delivery as a function of dose. An inflection occurred around 1 trillion nanoparticles (grey shaded zone, calculated using the limits of uptake by in vitro macrophages). Numbers indicate nanoparticle diameters, in nanometres. $R^2=0.74$. $n=6$ mice for 50 nm nanoparticles; $n=3$ mice for 15 nm and 100 nm nanoparticles. **b**, Liver accumulation as a function of dose behaved in an inverse pattern to the tumour, with inflection occurring at the same dose range. $R^2=0.86$. $n=6$ for 50 nm nanoparticles; $n=3$ mice for 15 nm and 100 nm nanoparticles. **c**–**j**, High doses increased tumour delivery (**c**,**e**,**g**,**i**) and reduced liver accumulation (**d**,**f**,**h**,**j**) in 4 mouse models: xenogeneic MDA-MB-231 mammary carcinoma in CD1 nude mice (**c**,**d**; low dose (0.2 trillion) $n=7$; high dose (50 trillion) $n=6$, across 2 independent experiments), transgenetic MMTV-PyMT mammary carcinoma in FVB/*n* mice (**e**,**f**; low-dose tumours $n=39$, livers $n=4$; high dose tumours $n=40$, livers $n=3$, across 2 independent experiments), xenogeneic U87 glioma in CD1 nude mice (**g**,**h**; $n=3$ across 1 experiment) and orthotopic 4T1 in CD1 nude mice (**i**,**j**; $n=3$ across 1 experiment). **k**,**l**, High doses increased tumour delivery and reduced liver accumulation in two different nanoparticle types: fluorescently-labelled silica nanoparticles (**k**, $n=3$ mice across 1 experiment) and radiolabelled liposomes (**l**, $n=5$ mice low dose, $n=6$ mice high dose, across 1 experiment). In **k**, a medium dose (3.1 trillion) was chosen because the fluorophore conjugation efficiency on silica particles was too low to be measured using the low dose. All bars and error bars represent mean ± s.e.m. Statistical significance was evaluated using a two-tailed unpaired *t*-test. $^*P<0.05$, $^{**}P<0.01$, $^{***}P<0.001$, $^{****}P<0.0001$. Exact *P* values for each panel are as follows: $P=0.00014$ (**c**); $P=0.042$ (**d**), $P=1.4\times10^{-8}$ (**e**), $P=0.026$ (**f**), $P=0.017$ (**g**), $P=0.019$ (**h**), $P=0.028$ (**i**), $P=0.045$ (**j**), $P=0.034$ (**k**) and $P=0.0080$ (**l**).

than surface area or mass as the dose effectively corresponds to the numbers of receptors that bind nanoparticles.

Overall, these results demonstrated that doses exceeding 1 trillion nanoparticles significantly increased tumour delivery for various nanoparticle sizes, compositions and tumour models.

Tumour cell delivery above the threshold dose

We also investigated the impact of the increased dose and delivery on nanoparticle interactions with cells in the tumour. The incomplete cellular delivery of cancer drugs is a general limitation. One reason is the difficulties of drugs diffusing across large distances[33]. Nanoparticles face similar challenges that may be further exacerbated by their larger sizes[34]. We hypothesized that a higher delivery efficiency would lead to a larger nanoparticle concentration gradient in the tumour that would ultimately facilitate more cellular interaction. Three-dimensional CLARITY imaging confirmed our hypothesis. We imaged nanoparticles near blood vessels[35,36] and observed that higher doses of nanoparticles beyond the trillion threshold were distributed further from blood vessels and deeper into the tumour tissues (Fig. 4a,b). High doses were well distributed throughout tumour cells (Fig. 4c) and mostly intracellular (Fig. 4d). Quantification with flow cytometry showed that 93%

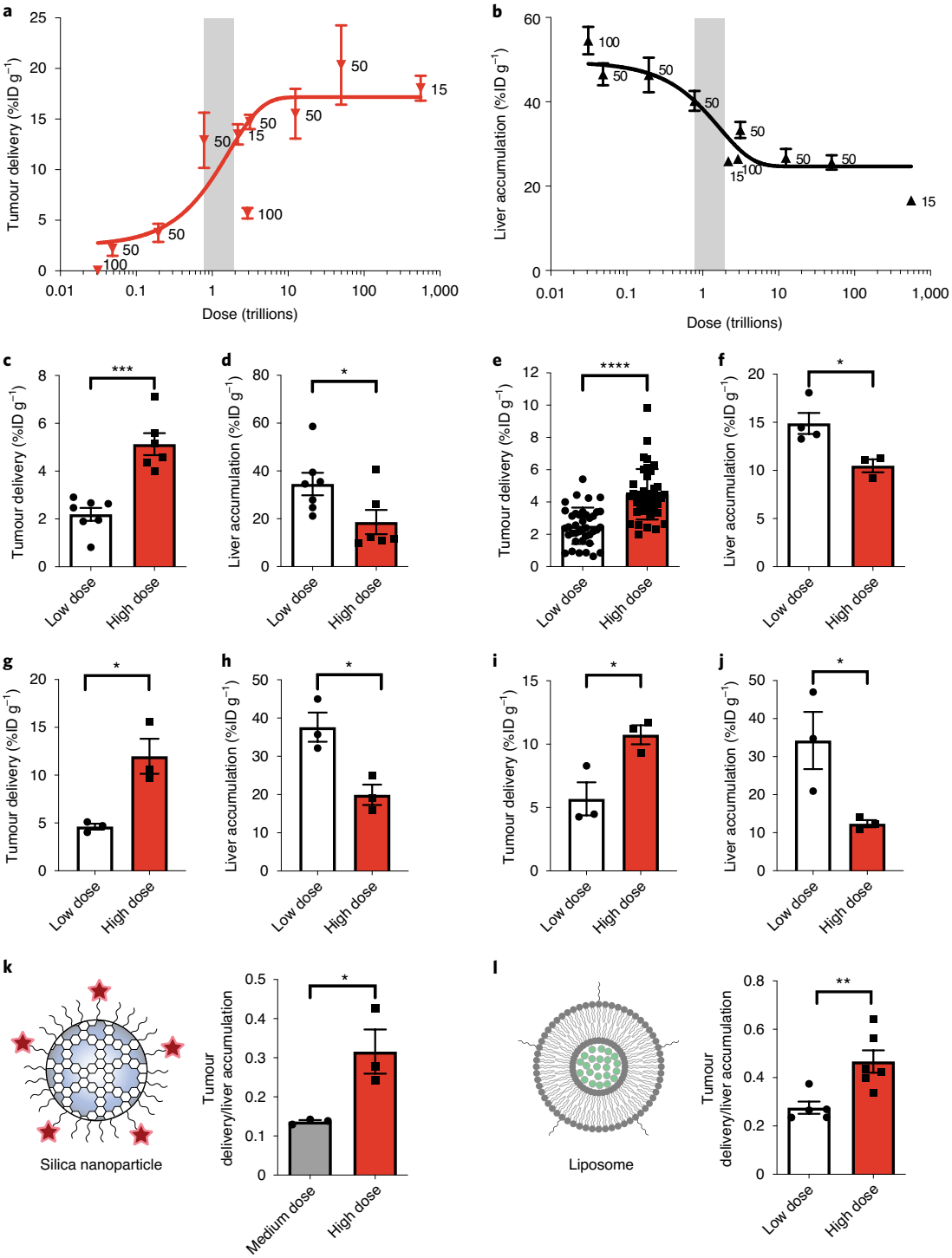

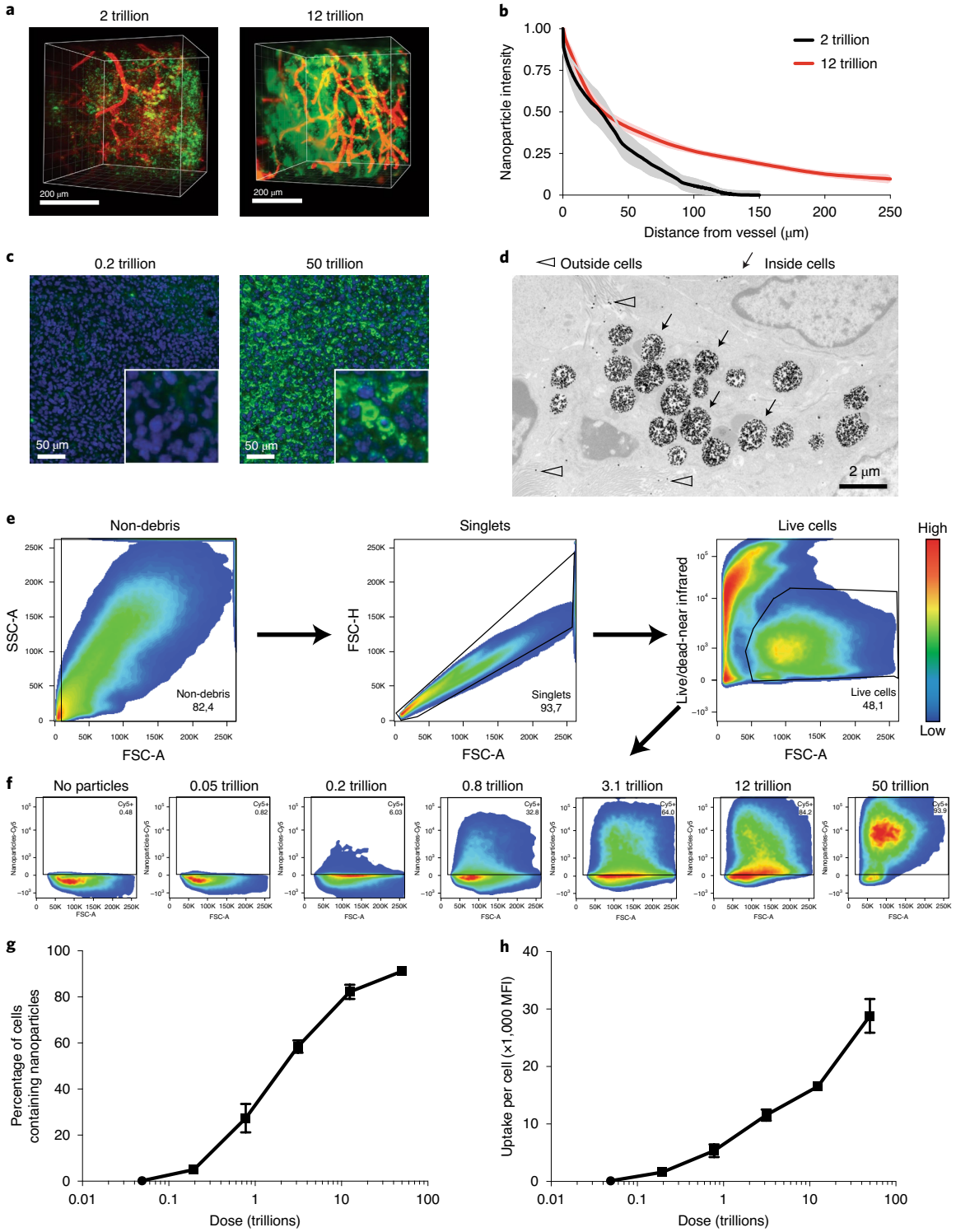

Fig. 4 | Tumour penetration and cell delivery above the threshold. a, Representative 3D volumes of tumours of mice injected with 2 trillion (left) or 12 trillion (right) nanoparticles. Blood vessels are in red and nanoparticles in green. **b**, Nanoparticle diffusion distance from the walls of blood vessels for 2 and 12 trillion nanoparticles. Intensity was normalized to the intensity at the vessel wall. $n=4$ samples from 2 mice for the 2 trillion dose. $n=6$ samples from 3 mice for the 12 trillion dose. Lines and shaded envelopes represent the mean ± s.e.m. **c**, Representative histology sections of the tumours of mice injected with a low dose (left, 0.2 trillion) or a high dose (right, 50 trillion) of nanoparticles after 24 h of circulation. Nuclei are in blue (fluorescence) and nanoparticles in green (dark-field imaging). Insets: ×3 magnification. **d**, Representative transmission electron microscopy image of tumours of mice injected with a high dose of nanoparticles after 24 h of circulation. Most nanoparticles were intracellular. **e**, Flow cytometry gating strategy for investigating cells that took up nanoparticles. **f**, Representative flow cytometry plots of live cells in the tumour that took up nanoparticles as a function of dose. **g**, Quantification of flow cytometry plots in **f** for the proportion of live cells in the tumour that took up nanoparticles as a function of dose. $n=3$ mice. **h**, The amount of nanoparticles taken up per cell. $n=3$ mice. Data points and error bars represent mean ± s.e.m.

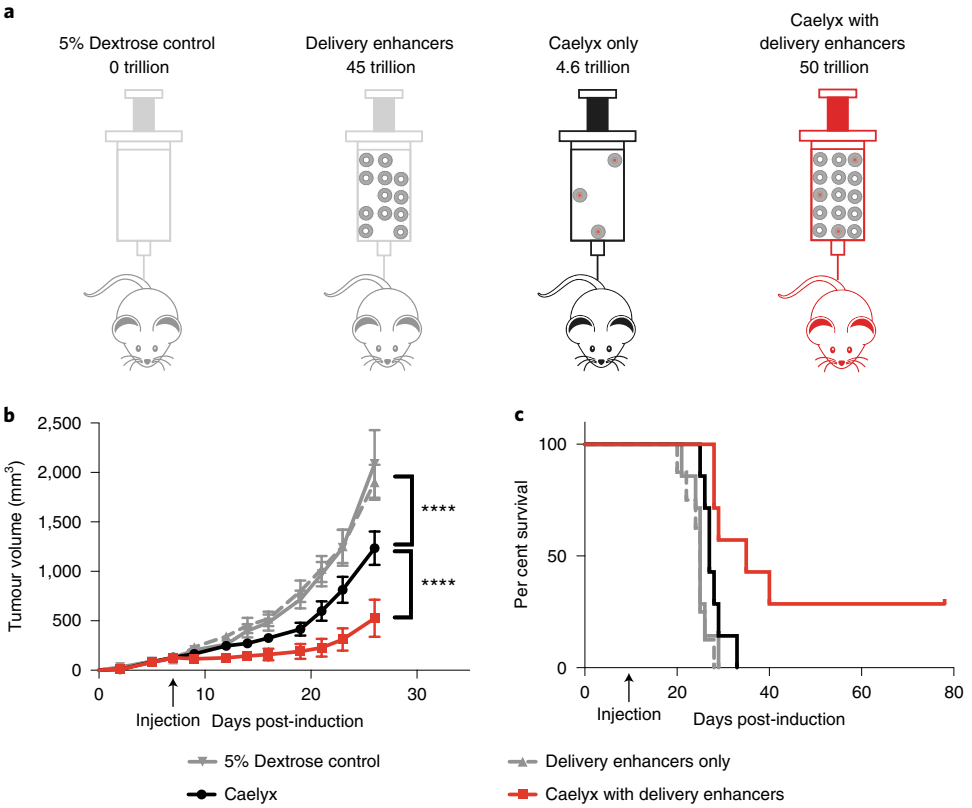

Fig. 5 | Therapeutic efficacy of Caelyx above the threshold. a, 4T1 tumour-bearing mice were injected with either 4.6 trillion Caelyx liposomes only or 4.6 trillion Caelyx liposomes with 45 trillion delivery enhancers. Control mice were injected with either 5% dextrose or delivery enhancers only. **b**, Mice treated with delivery enhancers had smaller tumours. $n=7$. Data points and error bars represent mean ± s.e.m. Statistical significance was evaluated using a two-way ANOVA with multiple comparisons with Bonferroni adjustment. $^{****}P<0.0001$. **c**, Mice treated with delivery enhancers survived longer than mice injected with Caelyx alone. $n=7$. Statistical significance was evaluated using a two-tailed Mantel–Cox log-rank test. Caelyx with delivery enhancers was statistically different from Caelyx only. Exact P values are as follows: delivery enhancers versus 5% dextrose $P=1$, Caelyx versus 5% dextrose $P=8.6\times10^{-8}$, Caelyx + delivery enhancers versus 5% dextrose $P=1\times10^{-15}$, Caelyx + delivery enhancers versus Caelyx $P=2.5\times10^{-5}$ (**b**); $P=0.0002$ (**c**).

of live cells had taken up nanoparticles at a high dose (Fig. 4e–g) and that each cell had taken up more nanoparticles (Fig. 4e,f,h). In contrast, a below-threshold low dose of nanoparticles (0.2 trillion) was sparsely distributed through the tumour tissue and only 0.7% of cells had internalized them (Fig. 4c–f). These results showed that administering numbers of nanoparticles above the threshold enhanced nanoparticle tumour penetration and improved delivery to the tumour cell population.

Above-threshold dosing improves therapeutic efficacy

We tested our theory of nanoparticle dosing using the cytotoxic nanoparticle Caelyx/Doxil. They were toxic and ablated liver Kupffer cells (Supplementary Figs. 19 and 20), which has been previously shown to confound their pharmacokinetics[37,38]. To untangle the effects of nanoparticle number dose versus drug dose, we therefore opted to artificially increase the nanoparticle dose using a benign filler nanoparticle to increase nanoparticle number dose without increasing the cytotoxic drug. We chose PEGylated liposomal doxorubicin (Caelyx/Doxil) as the therapeutic nanoparticle because Caelyx is clinically approved for a variety of cancers and has demonstrated therapeutic activity in the 4T1 tumour model[39]. We synthesized this benign filler nanoparticle to be identical to Caelyx but without loading any doxorubicin (Supplementary Fig. 16). We henceforth refer to them as delivery enhancers, because their only function was to artificially increase the number of nanoparticles to increase tumour delivery.

We designed a proof-of-concept efficacy experiment comparing two 4T1 tumour-bearing mouse groups that received the same dose of a therapeutic nanoparticle, but with the experimental group receiving an additional dose of delivery enhancers. Both groups received over 1 trillion nanoparticles to ensure significant dose-dependent delivery. The control group was injected with 4.6 trillion Caelyx nanoparticles (2 mg doxorubicin per kg), and the experimental group was co-injected with an additional 45 trillion delivery enhancers (50 trillion nanoparticles in total) (Fig. 5a). Although both groups received the same amount of active drug, we expected the experimental group to have greater efficacy because the delivery enhancers would improve tumour delivery efficiency of all nanoparticles, including Caelyx. We observed that the experimental group with delivery enhancers had higher serum and tumour levels of doxorubicin and greater numbers of doxorubicin-positive nuclei compared with mice treated with Caelyx alone up to 4 days post-injection (Supplementary Fig. 21). Compared with the mice treated with Caelyx alone, the mice treated with co-injected delivery enhancers had tumours that were 57% smaller (Fig. 5b and Supplementary Fig. 22) and survived 29% longer from a median of 27 days to 35 days (Fig. 5c). The use of a dose above the threshold was therefore critical to the therapeutic effectiveness of the nanoparticle. Negative control mice given only delivery enhancers saw no difference in efficacy compared with mice given a sugar water control, indicating that these delivery enhancers had no antitumour efficacy on their own (Fig. 5a–c). These

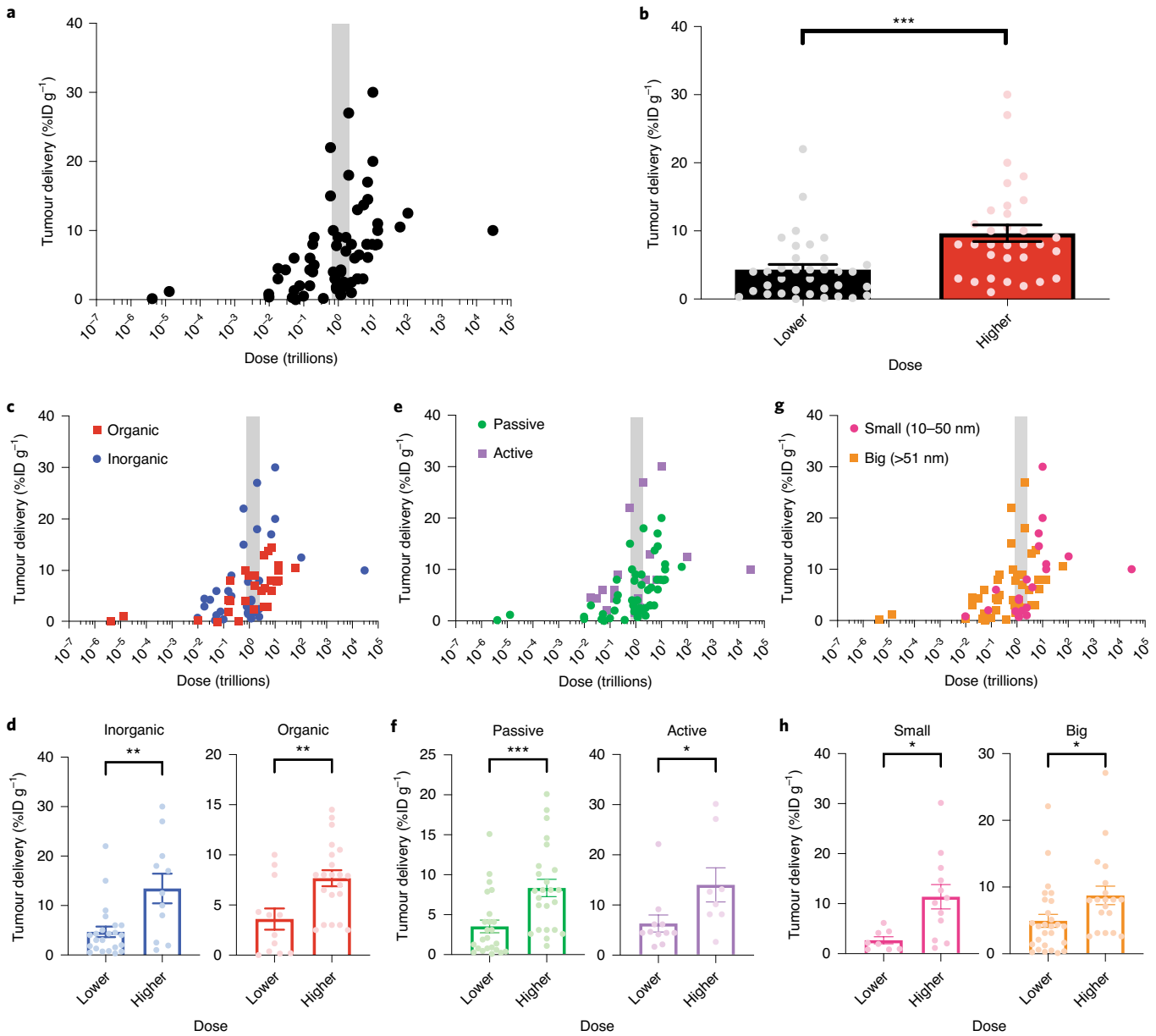

Fig. 6 | Identifying a dose threshold in publications from 2005–2015. Studies from the meta-analysis by Wilhelm et al[1]. were evaluated to identify a dose threshold. **a**, Tumour delivery as a function of dose across $n = 67$ data points from 40 publications between 2005 and 2015. There was a positive correlation between dose and tumour delivery ($R^2 = 0.39$, $P < 0.0001$). The grey bar represents in vitro uptake threshold described in Fig. 1d. **b**, The data in **a** were divided into two groups by the median dose of the publications: lower or higher than 1.2 trillion nanoparticles. **c**–**h**, The data from **a** and **b** were stratified according to organic versus inorganic classes of nanoparticles (**c**,**d**, $n = 33$ organic, $n = 34$ inorganic), passive versus active targeting nanoparticles (**e**,**f**, $n = 48$ passive, $n = 19$ active) and small versus big nanoparticles (**g**,**h**, $n = 20$ small, $n = 47$ big). Bars and error bars in **d**, **f** and **h** represent mean ± s.e.m. Lower and higher doses with respect to 1.2 trillion nanoparticles threshold. Statistical significance was evaluated using a two-tailed unpaired *t*-test. * $p < 0.05$, ** $p < 0.01$, *** $p < 0.001$. Exact *P* values are as follows: $P = 0.00030$ (**b**); inorganic $P = 0.0016$, organic $P = 0.0041$ (**d**); passive $P = 0.00080$, active $P = 0.042$ (**f**); small $P = 0.011$, big $P = 0.025$ (**h**).

delivery enhancers did not ablate additional Kupffer cells, so the prolonged circulation time was not due to destruction of the liver's clearance system (Supplementary Fig. 23). They did not cause acute (2 day), subacute (2 week) or chronic (1.4 yr) toxicity to the liver, heart or blood at this dose (Supplementary Figs. 24–34). Caelyx alone at higher doses (5 mg doxorubicin per kg and 10 mg doxorubicin per kg) completely ablated all Kupffer cells (Supplementary Fig. 20) and as such, delivery enhancers did not further improve therapeutic efficacy (Supplementary Figs. 35 and 36). We hypothesized that this was confounded because absent Kupffer cells would already minimize liver clearance so that increased nanoparticle numbers would not enhance tumour delivery efficiency further. We tested this by depleting Kupffer cells with clodronate liposomes before injecting below-threshold and above-threshold doses of gold nanoparticles. We observed that mice without Kupffer cells did not exhibit dose-dependent gold nanoparticle tumour delivery (Supplementary Fig. 37).

We also directly compared this threshold dosing principle with delivery enhancers to the RES blockade technique, which is a method that suffers from timing, material and dose selection

challenges[10,13,14,40–43]. Compared with sequential injections in the RES blockade, co-injection along the threshold principle led to improved pharmacokinetics, delivery efficiency and therapeutic efficacy (Supplementary Fig. 38). Furthermore, we observed that 50 trillion co-injected liposomes did not improve tumour delivery of 0.2 trillion gold nanoparticles (Supplementary Fig. 39) because these different nanoparticles accumulated in different Kupffer cells (Supplementary Fig. 40), probably due to different protein corona profiles (Supplementary Fig. 41)[44]. This suggested that Kupffer cells are a heterogenous population and that each cell clears a specific nanoparticle type. These results demonstrated that the dose threshold principle is more powerful than the RES blockade technique. Overall, our results proved that administering nanoparticle doses beyond the threshold directly improved therapeutic efficacy independently of the active drug dose.

The 1 trillion threshold exists throughout the literature

We sought to investigate the relevance of this threshold principle to the rest of the nanoparticle delivery field. In 2016, our group performed a meta-analysis of the field's delivery efforts and analysed all known parameters of nanoparticle design, including material, size, shape and surface chemistry, as well as differences in tumour models[1]. We did not include dose in the analysis. At that time, dose was not an obvious parameter that affected tumour delivery because it was not (and is still not) emphasized nor standardized in the literature.

We reanalysed that set of papers to investigate if the threshold persisted in other studies. We successfully recalculated nanoparticle doses by particle number in 40 publications and obtained 67 total data points of dose and delivery (Supplementary Tables 1 and 2). Using these calculations, we observed that dose by nanoparticle number correlated with delivery (Fig. 6a). We found that the median dose used in these papers was 1.2 trillion nanoparticles, near the 1 trillion threshold observed in our experiments. Doses higher than this threshold had significantly higher tumour delivery than doses below (Fig. 6b). We further stratified these data into inorganic versus organic, passive versus active and small (≤50 nm) versus big (>50 nm) nanoparticles and observed that this threshold persisted for all subdivisions (Fig. 6c–h). We also performed a multiple regression to predict tumour delivery from dose, material type, inorganic versus organic, targeting type, size (small versus big), tumour model, cancer type and specific cell line. This regression predicted tumour delivery ($F(8,55)=7.036$, $P=0.000002$; Supplementary Table 3a). Dose was the most significant variable in this regression ($P=0.00002$). This suggests that the number of nanoparticles contributes more to tumour delivery than size, targeting design, nanoparticle type or cancer model (Supplementary Table 3b). The importance of dose by nanoparticle number was clearly unknown in these papers because half of the studies used nanoparticle doses above the trillion threshold and half below, suggesting that doses were chosen arbitrarily. Additionally, none of these 117 papers rationalized their choice of dose, none directly reported the number of nanoparticles administered, and only 1 paper reported investigating more than one dose. These results emphasize that the relationship between nanoparticle dose by number and tumour delivery is significant but so far, unrealized. We urge the community to consider administering nanoparticles at doses above the threshold.

Discussion of clinical nanoparticles

We end with a brief discussion on clinical relevance to explore the potential of translating this threshold concept to human patients. Current nanoparticle dosing conventions in humans follow those used for small-molecule drugs, with doses assigned according to the amount of the active drug. For example, Caelyx is administered to humans at a recommended dose of 50 mg of doxorubicin per m^2, without mention of the equivalent dose of nanoparticles. The appropriate metric of nanoparticle or active pharmaceutical ingredient is controversial and debated[45,46]. We believe it would be beneficial to also describe administered dose in terms of the number of nanoparticles. Then we can estimate equivalent human threshold doses to our preclinical results. We start with the conceptual assumption that human liver and Kupffer cell clearance rates are also finite and can be overwhelmed beyond some threshold. The literature suggests that this can be extended to other mammals: liver mass extrapolation yields nanoparticle number thresholds in rats (8 trillion) and rabbits (63 trillion) and recalculated doses below this threshold have shown to be cleared rapidly by the liver[19,20]. This is in line with the threshold principle and thus our threshold discovery in mice may also apply to humans. A liver from an average 70 kg human weighs roughly 1,500 times more than a mouse liver. Extrapolating by mass and assuming similar Kupffer cell density and activity to mice, we estimate that human nanoparticle formulations should be administered at doses that exceed a threshold of 1,500 trillion nanoparticles (1.5 quadrillion) for meaningful tumour delivery. Typical doses of successful clinical nanoparticles such as Caelyx, Myocet and Onivyde exceed this threshold at 8.6, 1.7 and 1.9 quadrillion nanoparticles, respectfully. Interestingly, BIND-014 and NK105, investigational nanoparticles that fell short of clinical response targets, were dosed below this threshold at only 1 and 0.9 quadrillion per patient[47,48]. Notably, these particles were optimized for size, ligand density, drug encapsulation and release kinetics, without consideration of nanoparticle number dose[49]. A possible reason for the lack of efficacy could be because the nanoparticle doses were below threshold, leading to high sequestration into liver Kupffer cells and suboptimal delivery efficiency into tumours. This dosing threshold concept may also extend beyond cancer nanomedicine. In a phase II clinical trial, an adeno-associated virus therapy for hemophilia A similarly showed no detectable therapeutic effect in humans at a below-threshold 0.4 quadrillion viral particle dose but showed lasting therapeutic effect when dosed beyond 4.2 quadrillion particles[50]. The phase III study is investigating the efficacy at a dose of 2.8 quadrillion (clinical trial NCT03392974) – which we expect to be effective because it surpasses our proposed human threshold of 1.5 quadrillion. Future studies should investigate the role of dose using nanoparticle numbers as the metric on the efficacy of clinical nanomedicines.

Conclusion

We discovered a nanoparticle number threshold dose that improves nanoparticle delivery and therapy. Here we observed that a general threshold of 1 trillion nanoparticles overwhelmed the liver and maximized delivery to tumours to 12% of the injected dose in mice. This specific value may vary between nanoparticle designs and in vivo species, but it forms a foundational dose threshold concept for nanoparticle delivery for nanoparticles larger than 10 nm. Future studies should investigate how different nanoparticle designs refine this threshold and modulate delivery beyond it, which Kupffer cell receptors become overwhelmed and which biological tumour mechanisms dominate at high doses to increase tumour entry[51]. Towards immediate translation, current clinically approved anticancer nanoparticle formulations such as Caelyx/Doxil could adopt delivery enhancer strategies to improve delivery and therapeutic efficacy against solid tumours. Infusion reactions may be a concern with high nanoparticle doses, but can be prevented with proper prophylaxis and monitoring[52,53]. We envision that broad and careful evaluation of nanoparticle dose with respect to this threshold would provide a powerful, universal and simple method to advance a new generation of delivery strategies for imaging, diagnostics and therapy.

Online content

Any methods, additional references, Nature Research reporting summaries, source data, extended data, supplementary information, acknowledgements, peer review information; details of

author contributions and competing interests; and statements of data and code availability are available at https://doi.org/10.1038/s41563-020-0755-z.

Received: 12 July 2019; Accepted: 30 June 2020;
Published online: 10 August 2020

References

1. Wilhelm, S. et al. Analysis of nanoparticle delivery to tumours. *Nat. Rev. Mater.* **1**, 16014 (2016).
2. Rahman, Y. E., Cerny, E. A., Patel, K. R., Lau, E. H. & Wright, B. J. Differential uptake of liposomes varying in size and lipid composition by parenchymal and Kupffer cells of mouse liver. *Life Sci.* **31**, 2061–2071 (1982).
3. Perrault, S. D., Walkey, C., Jennings, T., Fischer, H. C. & Chan, W. C. W. Mediating tumor targeting efficiency of nanoparticles through design. *Nano Lett.* **9**, 1909–1915 (2009).
4. Arnida, Janát-Amsbury, M. M., Ray, A., Peterson, C. M. & Ghandehari, H. Geometry and surface characteristics of gold nanoparticles influence their biodistribution and uptake by macrophages. *Eur. J. Pharm. Biopharm.* **77**, 417–423 (2011).
5. Huang, X. et al. The shape effect of mesoporous silica nanoparticles on biodistribution, clearance, and biocompatibility in vivo. *ACS Nano* **5**, 5390–5399 (2011).
6. Juliano, R. L. & Stamp, D. The effect of particle size and charge on the clearance rates of liposomes and liposome encapsulated drugs. *Biochem. Biophys. Res. Commun.* **63**, 651–658 (1975).
7. Albanese, A., Tang, P. S. & Chan, W. C. W. The effect of nanoparticle size, shape, and surface chemistry on biological systems. *Annu. Rev. Biomed. Eng.* **14**, 1–16 (2012).
8. Tavares, A. J. et al. Effect of removing Kupffer cells on nanoparticle tumor delivery. *Proc. Natl Acad. Sci. USA* **114**, E10871–E10880 (2017).
9. Wolfram, J. et al. A chloroquine-induced macrophage-preconditioning strategy for improved nanodelivery. *Sci. Rep.* **7**, 1–13 (2017).
10. Proffitt, R. T. et al. Liposoinal blockade of the reticuloendothelial system: improved tumor imaging with small unilamellar vesicles. *Science* **220**, 502–505 (1983).
11. Cheng, Y.-H., He, C., Riviere, J. E., Monteiro-Riviere, N. A. & Lin, Z. Meta-analysis of nanoparticle delivery to tumors using a physiologically based pharmacokinetic modeling and simulation approach. *ACS Nano* **14**, 3075–3095 (2020).
12. Zhang, Y.-N., Poon, W., Tavares, A. J., McGilvray, I. D. & Chan, W. C. W. Nanoparticle–liver interactions: cellular uptake and hepatobiliary elimination. *J. Control. Release* **240**, 332–348 (2016).
13. Liu, T., Choi, H., Zhou, R. & Chen, I. W. RES blockade: a strategy for boosting efficiency of nanoparticle drug. *Nano Today* **10**, 11–21 (2015).
14. Sun, X. et al. Improved tumor uptake by optimizing liposome based RES blockade strategy. *Theranostics* **7**, 319–328 (2017).
15. Drummond, D. C., Noble, C. O., Hayes, M. E., Park, J. W. & Kirpotin, D. B. Pharmacokinetics and in vivo drug release rates in liposomal nanocarrier development. *J. Pharm. Sci.* **97**, 4696–4740 (2008).
16. Tsoi, K. M. et al. Mechanism of hard-nanomaterial clearance by the liver. *Nat. Mater.* **15**, 1212–1221 (2016).
17. Iio, M. & Wagner, H. N. Studies of the reticuloendothelial system (RES). I. Measurement of the phagocytic capacity of the RES in man and dog. *J. Clin. Invest.* **42**, 417–426 (1963).
18. Allen, T. M. & Hansen, C. Pharmacokinetics of stealth versus conventional liposomes: effect of dose. *BBA Biomembr.* **1068**, 133–141 (1991).
19. Laverman, P. et al. Preclinical and clinical evidence for disappearance of long-circulating characteristics of polyethylene glycol liposomes at low lipid dose. *J. Pharmacol. Exp. Ther.* **293**, 996–1001 (2000).
20. Utkhede, D. R. & Tilcock, C. P. Effect of Lipid dose on the redistribution and blood pool clearance kinetics of PEG-modified technetium-labeled lipid vesicles. *J. Liposome Res.* **8**, 381–390 (2008).
21. Kai, M. P. et al. Tumor presence induces global immune changes and enhances nanoparticle clearance. *ACS Nano* **10**, 861–870 (2016).
22. Bouwens, L., Baekeland, M., de Zanger, R. & Wisse, E. Quantitation, tissue distribution and proliferation kinetics of Kupffer cells in normal rat liver. *Hepatology* **6**, 718–722 (1986).
23. Lee, S.-H., Starkey, P. M. & Gordon, S. Quantitative analysis of total macrophage content in adult mouse tissues: immunochemical studies with monoclonal antibody F4/80. *J. Exp. Med.* **161**, 475–489 (1985).
24. Park, J.-K. et al. Cellular distribution of injected PLGA-nanoparticles in the liver. *Nanomedicine* **12**, 1365–1374 (2016).
25. Poon, W. et al. Elimination pathways of nanoparticles. *ACS Nano* **13**, 5785–5798 (2019).
26. Ishida, T. & Kiwada, H. Accelerated blood clearance (ABC) phenomenon upon repeated injection of PEGylated liposomes. *Int. J. Pharm.* **354**, 56–62 (2008).
27. Sasmono, R. T. et al. A macrophage colony-stimulating factor receptor-green fluorescent protein transgene is expressed throughout the mononuclear phagocyte system of the mouse. *Blood* **101**, 1155–1163 (2003).
28. Kolb-Bachofen, V., Schlepper-Schäfer, J. & Kolb, H. Receptor-mediated particle uptake by liver macrophages. *Exp. Cell Res.* **148**, 173–182 (1983).
29. Commisso, C. et al. Macropinocytosis of protein is an amino acid supply route in Ras-transformed cells. *Nature* **497**, 633–637 (2013).
30. Canton, J. et al. Calcium-sensing receptors signal constitutive macropinocytosis and facilitate the uptake of NOD2 ligands in macrophages. *Nat. Commun.* **7**, 11284 (2016).
31. Lazarovits, J. et al. Supervised learning and mass spectrometry predicts the in vivo fate of nanomaterials. *ACS Nano* **13**, 8023–8034 (2019).
32. Gordon, S. Phagocytosis: an immunobiologic process. *Immunity* **44**, 463–475 (2016).
33. Minchinton, A. I. & Tannock, I. F. Drug penetration in solid tumours. *Nat. Rev. Cancer* **6**, 583–592 (2006).
34. Sykes, E. A., Chen, J., Zheng, G. & Chan, W. C. W. Investigating the impact of nanoparticle size on active and passive tumor targeting efficiency. *ACS Nano* **8**, 5696–5706 (2014).
35. Kingston, B. R., Syed, A. M., Ngai, J., Sindhwani, S. & Chan, W. C. W. Assessing micrometastases as a target for nanoparticles using 3D microscopy and machine learning. *Proc. Natl Acad. Sci. USA* **116**, 14937–14946 (2019).
36. Syed, A. M. et al. Three-dimensional imaging of transparent tissues via metal nanoparticle labeling. *J. Am. Chem. Soc.* **139**, 9961–9971 (2017).
37. Gabizon, A., Tzemach, D., Mak, L., Bronstein, M. & Horowitz, A. T. Dose dependency of pharmacokinetics and therapeutic efficacy of pegylated liposomal doxorubicin (DOXIL) in murine models. *J. Drug Target.* **10**, 539–548 (2002).
38. Ohara, Y. et al. Effective delivery of chemotherapeutic nanoparticles by depleting host Kupffer cells. *Int. J. Cancer* **131**, 2402–2410 (2012).
39. Charrois, G. J. R. & Allen, T. M. Multiple injections of pegylated liposomal doxorubicin: pharmacokinetics and therapeutic activity. *J. Pharmacol. Exp. Ther.* **306**, 1058–1067 (2003).
40. Simberg, D. et al. Biomimetic amplification of nanoparticle homing to tumors. *Proc. Natl. Acad. Sci. USA* **104**, 932–936 (2007).
41. Souhami, R. L., Patel, H. M. & Ryman, B. E. The effect of reticuloendothelial blockade on the blood clearance and tissue distribution of liposomes. *Biochim. Biophys. Acta* **674**, 354–371 (1981).
42. Fernández-Urrusuno, R. et al. Effect of polymeric nanoparticle administration on the clearance activity of the mononuclear phagocyte system in mice. *J. Biomed. Mater. Res.* **31**, 401–408 (1996).
43. Wagner, H. N. & Iio, M. Studies of the reticuloendothelial system (RES). III. Blockade of the RES in man. *J. Clin. Invest.* **43**, 1525–1532 (1964).
44. Walkey, C. D., Olsen, J. B., Guo, H., Emili, A. & Chan, W. C. Nanoparticle size and surface chemistry determine serum protein adsorption and macrophage uptake. *J. Am. Chem. Soc.* **134**, 2139–2147 (2012).
45. Mcneil, S. E. Evaluation of nanomedicines: stick to the basics. *Nat. Rev. Mater.* **1**, 16073 (2016).
46. Wilhelm, S., Tavares, A. J. & Chan, W. C. W. Reply to "Evaluation of nanomedicines: stick to the basics". *Nat. Rev. Mater.* **1**, 16074 (2016).
47. Autio, K. A. et al. Safety and efficacy of BIND-014, a docetaxel nanoparticle targeting prostate-specific membrane antigen for patients with metastatic castration-resistant prostate cancer: a phase 2 clinical trial. *JAMA Oncol.* **4**, 1344–1351 (2018).
48. Fujiwara, Y. et al. A multi-national, randomised, open-label, parallel, phase III non-inferiority study comparing NK105 and paclitaxel in metastatic or recurrent breast cancer patients. *Br. J. Cancer* **120**, 475–480 (2019).
49. Hrkach, J. et al. Preclinical development and clinical translation of a PSMA-targeted docetaxel nanoparticle with a differentiated pharmacological profile. *Sci. Transl. Med.* **4**, 128ra39–128ra39 (2012).
50. Rangarajan, S. et al. AAV5–factor VIII gene transfer in severe hemophilia A. *N. Engl. J. Med.* **377**, 2519–2530 (2017).
51. Sindhwani, S. et al. The entry of nanoparticles into solid tumours. *Nat. Mater.* **19**, 566–575 (2020).
52. Szebeni, J., Simberg, D., González-Fernández, Á., Barenholz, Y. & Dobrovolskaia, M. A. Roadmap and strategy for overcoming infusion reactions to nanomedicines. *Nat. Nanotechnol.* **13**, 1100–1108 (2018).
53. La-beck, N. M. & Gabizon, A. A. Nanoparticle interactions with the immune system: clinical implications for liposome-based cancer chemotherapy. *Front. Immunol.* **8**, 6–11 (2017).

Methods

Nanomaterial synthesis. *Gold nanoparticles.* All glassware was cleaned using aqua regia (3:1 hydrochloric acid:nitric acid), dish soap and deionized water before use. Particles with 15 nm diameters were synthesized by adding 1 ml of 3% (w/v) sodium citrate tribasic dehydrate (Sigma S4641) to 98 ml of boiling deionized water under vigorous stirring, followed immediately by 0.1 ml of 10% (w/v) chloroauric acid tetrahydrate (Sigma 254169). This mixture was boiled and stirred for 7 min, and then immediately cooled in an ice water bath. The 50 and 100 nm particles were synthesized by seed-mediated growth[16]. The 50 nm particles were synthesized by chilling reagents in an ice bath: 750 ml deionized water, 9.475 ml of 10% (w/v) (250 mM) chloroauric acid tetrahydrate, 9.629 ml of 4.41% (w/v) (150 mM) sodium citrate tribasic dehydrate, 250 ml of 4 nM 15 nm particles and 9.629 ml of 2.75% (w/v) (250 mM) hydroquinone (Sigma H17902). The 100 nm particles were made by reducing the 250 ml of 15 nm particles to 23 ml of 15 nm and topping up with deionized water. The ice-cold reagents were added in the order listed above to a 2 l Erlenmeyer flask under vigorous stirring (note: hydroquinone was added as quickly as possible). The reaction proceeded overnight at 4 °C. Synthesized nanoparticles were washed twice in a wash buffer containing 0.02% (w/v) sodium citrate tribasic and 0.1% (w/v) Tween20. Washing proceeded as follows: 13 ml in a 15 ml centrifuge tube, centrifuged for 2 h at 1,500*g* (50 nm nanoparticles) or 500 g (100 nm nanoparticles). The supernatant was discarded and particles were resuspended in 40 ml of wash buffer under sonication in a water bath (Misonix 2510R-MT). This 40 ml was divided into 40 1.5 ml microcentrifuge tubes and centrifuged at the same speeds for 45 min. The supernatant was discarded and the particles resuspended in a total of 6 ml of wash buffer under sonication. Particles were PEGylated by mixing methoxy-terminated 5 kDa polyethylene glycol thiol (Laysan Bio Inc) and amine-terminated 10 kDa polyethylene glycol thiol (Rapp Polymere GmbH) at a 4:1 ratio. This mixture was added to the nanoparticles at a ratio of 5 PEG per nm^2 and incubated at 60 °C for 30 min. These PEGylated particles were washed three times in Eppendorf tubes with wash buffer (50 nm: 2,500*g* for 45 min). In the last step, the supernatant was replaced with 0.5 ml of 0.1 M sodium bicarbonate. Sulfo-Cy5-NHS dye (Click Chemistry Tools 1076–100) was added at a molar ratio of 2:1 relative to amine PEG and rotated at 4 °C overnight. The particles were then washed three times in PBS plus 0.1% (w/v) Tween20, and twice in PBS. Particles were characterized by dynamic light scattering, TEM and UV–visible spectroscopy (Supplementary Fig. 1).

Silica nanoparticles. Five milligrams of 5 kDa ortho-pyridyl disulfide succinimidyl valerate OPSS-PEG-SVA (Laysan Bio) and 19.8 mg of 5 kDa SVA-mPEG (Laysan Bio) were weighed and dissolved in a total of volume of 250 µl of 10 mM HEPES buffer and 1 mM NaCl. This PEG solution was mixed with 500 µl of 50 nm aminated silica nanoparticles (nanoComposix SIAN50–25M), vortexed and incubated at 60 °C for 1 h. The solution was centrifuged at 10,000*g* for 45 min and washed twice more with HEPES (pH 7.44) at 8,500*g* for 45 min. Then 500 µl of 10 mM Tris-2-carboxyethyl phosphine (TCEP) in HEPES was transferred to resuspend the pellet of SiNPs, and the solution was kept at 60 °C for 30 min. It was washed twice by centrifugation at 8,000*g* in 500 µl of HEPES. SiNPs were mixed with 100 µg of sulfo-Cy5-maleimide at room temperature overnight. The next day, this was washed twice with HEPES and 0.05% (w/v) Tween-20. Particles were characterized by dynamic light scattering, TEM, UV–visible spectroscopy and fluorimetry (Supplementary Fig. 15).

Radiolabelled liposomes. Liposomes were synthesized as described in earlier work[1] with modifications. Briefly, 45.2 mg of hydrogenated soy phosphatidylcholine (Avanti 840058), 16.3 mg of cholesterol (Sigma C8667) and 14.8 mg of 1,2-distearoyl-sn-glycero-3-phosphoethanolamine-*N*-[amino(polyethylene glycol)-2000] (DSPE-PEG2000; Avanti 880128P) (molar ratio HSPC:CHOL: DSPE-PEG2000 = 55:40:5) were dissolved in chloroform and dried to a lipid film under a gentle stream of nitrogen. The lipid film was hydrated in HEPES (10 mM HEPES, 150 mM NaCl, pH 4.0) containing 10 mM of DOTA (1,4,7,10-Tetraazacyclododecane-1,4,7,10-tetraacetic acid (Aldrich 86734)). The lipid suspension, with total lipid concentration of 15 mg ml^{-1}, was sonicated in a glass vial for 5 min, and then subjected to 9 freeze–thaw cycles (freezing the test tube in liquid nitrogen and thawing it in water at 70 °C). The liposome suspension was extruded 9 times using a LIPEX TM high pressure liquid extruder through a 100-nm pore size polycarbonate membrane at 70 °C. The formed liposome was subjected to a repeated spin filtration process to remove unencapsulated external DOTA by buffer exchanging. Briefly, 0.5 ml of liposomes (15 mg ml^{-1}) were diluted with HEPES (10 mM, 150 mM NaCl, pH 4.0) to a total volume of 12 ml, loaded on a Amicon Ultra-15 centrifugal filter units (100 kDa cutoff), and centrifuged at 4,000 r.p.m. to remove 11 ml of the buffer solution. The spin filtration was repeated four times, and the purified DOTA-encapsulated liposomes were collected. Immediately before the radiolabelling, the purified liposome with pH 4.0 passed through a 7 K MWCO Zeba desalting spin column that was pre-saturated with a HEPES saline buffer with pH 7.4 (10 mM, 150 mM NaCl) to give the liposome pH gradient (pH 4 inside liposome, pH 7.4 outside particles). These liposomes were characterized by dynamic light scattering to have a mean size of 96 nm and polydispersity index (PDI) 0.062 (Supplementary Fig. 16) and were used immediately for ^{64}Cu labelling.

Liposome ^{64}Cu radiolabel loading. For quantification, liposomes were radiolabelled with ^{64}Cu following a previously described unassisted loading technique[54]. Aqueous ^{64}CuCl (Washington University School of Medicine) was diluted in HEPES buffered saline (pH 7.4) and mixed with different amounts of freshly prepared, buffer-exchanged liposomes. The remote loading process was conducted at 50 °C for up to 70 min under constant stirring. After loading, the liposomes and free ^{64}Cu were separated using filter centrifugation (Amicon Ultra 10 kDa 0.5 ml centrifugal filter unit, EMD Millipore). The HEPES buffered saline was exchanged until activity could no longer be detected in the eluent. The radiolabelling efficiency was calculated as the ratio of the concentrate activity divided by the sum of the concentrate and eluent activities, here ranging from 77% for the low liposome dose to 98% for the high liposome dose.

Animal models. All animal research was reviewed by and conducted in accordance with the animal ethics committee from the Division of Comparative Medicine at the University of Toronto (protocols numbers 20011909, 20012099 and 20011605) and the Animal Resources Centre at the University Health Network (protocol number 6040). Animals were housed at an ambient temperature of 22 °C (22–24 °C) and humidity of 45%, with a 14/10 day/night cycle (on at 6:00, off at 20:00), and allowed access to food ad libitum. The six-week-old female BALB/c mice were purchased (Charles River Laboratory BALB/cAnNCrl). 4T1 cells were a gift from R. Gorczynski and also purchased from ATCC (ATCC CRL-2539). 4T1 tumours were induced as described in earlier work[55] into 7-week-old mice. Briefly, 1 million 4T1 cells between passages 3–20 in 100 µl of serum-free, antibiotic-free RPMI (Wisent Bioproducts 350–000-EL) were injected into the right inguinal fifth mammary fat pad using a 25 G needle. The needle was inserted 1 mm lateral and 3 mm caudal to the nipple, and advanced towards the nipple by 2 mm. Mice were injected with nanoparticles 2 weeks post-induction unless specified otherwise. We aimed to investigate smaller tumours to minimize confounding effects from the necrotic core and to maximize quantification accuracy. Tumour growth was homogeneous (average 14-day tumour size and standard deviation: 0.38 ± 0.15 g). Tumours were size-matched between treatment groups to enable percentage of the injected dose (%ID) and %ID g^{-1} comparisons between groups. MMTV-PyMT transgenic mice on FVB/n background were purchased as a breeding pair (Jackson Laboratories 002374). Offspring were sent for genotyping from 3 mm tail snips using real-time polymer chain reaction at TransnetYX. Female heterozygous mice were injected with nanoparticles while they were between 10 and 13 weeks old (tumours ~580 ± 470 mm^3). Six-week-old CD1 nude mice were purchased (Charles River Laboratory Crl:CD1-*Foxn1*^{nu}). Cancer cells were injected orthotopically into the mammary glands as above: 8 million MDA-MB-231 cells between passages 2–5 in 200 µl of a mix of 50% (v/v) Dulbecco's minimal essential medium (DMEM; with 10% (v/v) fetal bovine serum and 1% (v/v) penicillin/streptomycin) and 50% (v/v) Matrigel (Fisher Scientific CB-40234), or 1 million 4T1 cells as above. U87-MG cells were a gift from G. Zheng and are commercially available from ATCC (ATCC HTB-14). 5 million U87-MG cells were injected into the subcutaneous flank of CD1 nude mice in a mix of 50% (v/v) DMEM (with 10% (v/v) fetal bovine serum and 1% (v/v) penicillin/streptomycin) and 50% (v/v) Matrigel (Fisher Scientific CB-40234). Mice were injected with nanoparticles while they were between 12 and 14 weeks old (tumours ~300 mm^3). Transgenic BALB/c mice expressing EGFP on cells expressing CSF-1R (Csf1r-EGFP; also c-fms-EGFP) were bred from a breeder pair gift from M. Egeblad, and were first created by D. Hume's lab[27].

Gold nanoparticle biodistribution. Mice were euthanized by isoflurane overdose followed by cervical dislocation at 2, 8, 24 or 72 h post nanoparticle injection. Mouse organs were collected and weighed into borosilicate tubes for analysis by ICP-MS[8,56]. Collected organs included: heart, lungs, liver, spleen, stomach (with diet), large intestines (with diet), small intestines (with diet), kidneys, uterus, dorsal skin and cardiac blood. For endpoint cardiac blood, mice hearts were quickly exposed by dissecting through the thoracic cavity. A 25 G needle/1 ml syringe was inserted into the right ventricle of the beating heart. Approximately 600 µl of cardiac blood was drawn then transferred to a glass tube. For reference, a control tube containing a known proportion of the injected dose was also prepared in a borosilicate tube. Then 800 µl of 16 M nitric acid (Caledon 7525–1–29) was added to each sample. The samples were digested at 80 °C in a water bath for 1 h, and then digested overnight at 50 °C. The next morning, 200 µl of 12 M hydrochloric acid (Caledon 6025–1–29) was added and the samples were digested at 80 °C for ≥1 h. Samples were collected into polypropylene 50 ml centrifuge tubes (Biomart 110708) and then diluted to 40 ml in deionized water for a final acid concentration of 2.5% (v/v); 10 ml of these samples was then filtered through a 0.22 µm PES filter (Fisher Scientific SLGP033RS) into 15 ml centrifuge tubes (Sarstedt 62.554.002). A standard curve for elemental gold and magnesium was prepared by dilution in 2% (v/v) nitric acid and 0.5% (v/v) hydrochloric acid, with concentrations ranging from 0.0001 to 100 mg ml^{-1}, with a reference blank of 0 mg ml^{-1}. All samples were then quantified using a NexION 350x ICP-MS (PerkinElmer) with mass analyser set to magnesium Mg 24, iridium Ir 192, and gold Au 197. A 500 µl injection loop was used, and each sample was mixed with a carrier solution (2% (v/v) nitric acid) and iridium internal standard (1 µg ml^{-1}) before injection into the analyser. The %ID was the measured gold mass of each sample divided by the measured gold mass of the injected dose.

Blood collection and gold quantification. For blood half-life studies, mouse tail veins were punctured using a 29 G needle and bled at various time points for repeated measurements of each mouse. Then 5–10 µl of blood was collected in capillary tubes (Fisher 2120–22260950) and transferred to 1.5 ml centrifuge tubes (Fisher 14222155). All blood was weighed and stored at 4 °C until further analysis. Then 200 µl of 16 M nitric acid and 50 µl of 12 M hydrochloric acid were added in sequence. These samples were then diluted into 9.75 ml of deionized water. Samples were not filtered to prevent gold adsorption and loss onto the filter. Samples were analysed by ICP-MS as described above.

In vitro saturation. RAW264.7 cells were seeded into a 24-well non-tissue cultured treated plates (Falcon 351147) at a density of 136,000 cells in 333 µl of DMEM media. Immediately after, 50 nm gold nanoparticles (concentration range: 0.25–4 nM) with a 5 kDa methyl-PEG-SH surface density of 0.17 PEG per nm^2 were added to the wells and cells were exposed for 24 h. At the end of the experiment, wells were gently washed with calcium-free PBS three times. Then cells were removed from the wells by vigorous pipetting and pelleted in a 1.5 ml centrifuge tube. The supernatant was frozen, and the pellets were frozen at −20 °C until analysis. ICP-MS was performed as previously described[6] to determine the amount of gold in each pellet. Pellets were digested with 800 µl of nitric acid and 200 µl hydrochloric acid, then number of cells was determined through magnesium concentration, compared with the magnesium concentration of a sample of a known number of cells. The mass of gold per cell was converted into particles per cell using the density of gold (19 g cm^{-3}).

Intravital microscopy. *Intravital microscopy preparation.* Csf1r-EGFP BALB/c mice were used between 8 and 11 weeks of age. Anaesthesia in mice was induced with 5% isoflurane in humidified oxygen, and maintained at 2.5–3.0% isoflurane. Anesthetized mice were shaved on their abdomen and placed supine onto a warmed heat pad. A skin incision was made mid-abdomen and extended superiorly past the xyphoid process. The fascia between the skin and peritoneum was blunt-dissected. Excess fur was wiped away with sterile PBS-soaked cotton swabs. An incision was made just inferior to the xyphoid process in the peritoneum, and extended superiorly to mid-thorax. Longitudinal blood vessels in the peritoneum were cauterized before lateral incisions were made. The liver was exposed and gently pulled inferiorly with a sterile cotton swab to expose the falciform ligament. The falciform ligament was cut. The mouse was placed onto its right side, and the left liver lobe was gently pulled out of the abdominal cavity and onto a platform. Care was taken not to disturb the superior aspect of the lobe, which was to be imaged. A few drops of sterile PBS were applied onto the liver surface. A number 1 glass slide (Fisherbrand 12544E) was gently placed onto the liver with care to not compress sinusoids. A drop of PBS was placed between a water-immersion lens and glass slide. Wide-field fluorescent imaging was performed under the fluorescein isothiocyanate (FITC) filterset to confirm blood flow in sinusoids. Periportal Kupffer cells were identified as $EGFP^+$ cells near the source point of divergent sinusoids. A 29 G needle loaded with injection solution was inserted into a lateral tail vein, to be injected after recording began.

Intravital microscopy imaging. Microscopy was performed using a Zeiss LSM 710 confocal microscope on an upright AxioExaminer stand with a ×20, 1.0 numerical aperture (NA) water-immersion Plan Apochromat objective lens. EGFP, Cy3, and Cy5 were excited using 488 nm, 561 nm and 633 nm laser lines, and detected with emission windows 493–556 nm and 638– 759 nm. The laser power was set between 2 and 10%, and the gain was manually adjusted to maximize the signal-to-noise ratio. The confocal pinhole size was set to 1–2 Airy units. Images were collected at a rate of 1 image every 3 s with a resolution of 512 pixels × 512 pixels, and averaging 2 scans per line. The laser scan speed was set to 1.5 s per frame with bidirectional raster scanning. Two to 5 min of video were pre-recorded before nanoparticles were injected to establish a baseline. Recording continued up to 45–60 min after injection.

Intravital microscopy analysis. Images were processed using ImageJ/FIJI[57] version 2.0.0-rc-69/1.52p. Macrophages were manually traced and masked from the EGFP channel. Nanoparticles were quantified using this mask in the Cy3 or Cy5 channels at 2, 5, 10, 15 and 25 min post-injection. Breathing artefacts during imaging often created dark bands across the image; such dark spots were replaced using Adobe Photoshop[58] by cutting and pasting time-adjacent frames to form a complete cell image. Uptake rates were calculated as average slopes from the uptake versus time values.

Silica nanoparticle quantification. Mouse organs were imaged in a Kodak in vivo Multispectral Imaging System (Bruker Corporation). Excitation and emission filters of 650 nm and 700 nm were used with an exposure time of 10 min. ImageJ/FIJI was used to obtain the signal density of tumours and livers. The tumour/liver ratio was obtained by dividing the tumour signal density by the liver signal density of each mouse, and then obtaining an average of the ratios.

Liposome ^{64}Cu biodistribution. Radiolabelled liposomes were terminally sterilized using a 0.22 µm syringe filter (Milles-GP Sterile Syringe Filters with PES Membrane, EMD Millipore). Injections were prepared with volumes between 200 and 250 µl in 31 G needles (BD Insulin Syringe with Ultra Fine Needle 31 G, BD). The activity of each injection was assessed with a dose calibrator (CRC-15R Enhanced, Capintec). The radioactive doses were 3.472 ± 0.123 MBq and 38.214 ± 0.888 MBq for the low- and high-liposome dose groups, respectively. Tumour-bearing mice were assigned to one of three liposome dose groups and injections were given via the lateral tail vein. The residual activity of each injection was assessed and used to correct for the injected dose per animal. At the required time point after radiolabelled liposome injection, mice were euthanized using a cardiac exsanguination technique and cervical dislocation under inhaled anaesthesia. A necropsy was performed and select tissues removed, including the whole blood, heart, lungs, liver, kidneys, spleen, stomach (including diet), large and small intestines (including diet), dorsal skin, tumour, tail and rest-of-body (ROB). The tissues were placed into pre-weighed plastic tubes (Sarstedt) and individually measured for activity using a gamma counting (Wallac Wizard 3"1480 Automatic Gamma Counter, PerkinElmer). The linear range of detection for ^{64}Cu activity was 0.31 kBq to 61.30 kBq. The final tissue weights were calculated, and the activity in each tissue corrected for ^{64}Cu decay to the time of liposome injection. Tissue biodistribution data were expressed as %ID in each tissue. All animal experiments performed with liposomes were in compliance with the University Health Network's guidelines for animal use (AUP Number 4299).

Liver histology. *Sinusoidal wall analysis.* 4T1 tumour-bearing mice were injected with one of two doses of nanoparticles (0.8 trillion and 50 trillion) through the tail vein. Mice were euthanized 15 min later. A midline abdominal incision was made to expose internal organs. Intestines were lifted out of the abdominal cavity to provide easier access to liver. The median lobe was excised and immersed in 10% neutral buffered formalin (Sigma HT501128). This lobe was fixed for 24 h at room temperature, then transferred to 70% ethanol solution for storage. Tissues were processed by the The Centre for Phenogenomics. Briefly, the liver was routinely processed and embedded in paraffin wax. Tissue sections cut at 5 µm were collected onto charged slides and baked before immunohistochemical staining. Tissue sections were deparaffinized through xylenes and an alcohol gradient and taken to water. Antigen retrieval was performed using heat-induced epitope retrieval with citrate buffer (pH 6) for 7 min. Non-specific antibody binding was blocked with Dako Protein block (Agilent X0909) for 10 min, followed by Armenian Hamster Anti-CD209b (ThermoFisher Scientific 14-2093-81) diluted at 1:200, and incubated overnight at 4 °C. After washes, goat anti-Armenian hamster alexafluor 488 (Abcam ab173003) secondary antibody diluted at 1:200 was used to visualize CD209b positive staining. This was imaged using an Olympus VS120 whole-slide imaging system at ×20 magnification in the FITC (CD209b) and dark-field (nanoparticles) channels. Images were visualized using ImageJ to identify vessels and nanoparticles. Nanoparticle distribution was performed using the Line tool drawn from one wall of a blood vessel to the other, and quantified using the Line Profile function of ImageJ. Twenty blood vessels were chosen at random per liver for a total quantification of 60 vessels per dose. The vessel widths were all expanded/normalized to the largest vessel width of the group, and the nanoparticle signals of smaller vessels were expanded to this size by interpolation using the interp1 function in MATLAB (MathWorks MATLAB R2019b)[59].

Liver cell analysis. 4T1 tumour-bearing were injected with doses of nanoparticles ranging from 50 billion to 50 trillion. Mice were euthanized 24 h later. The median lobe of the liver was dissected and cryopreserved in 'optimum cutting temperature' compound (VWR 25608–930) in indirect contact with liquid nitrogen. Histological slides were processed at the The Centre for Phenogenomics. Briefly, 8-µm-thick sections were sectioned on a Cryostar NX70 cryostat. The tissue was stained with anti-F4/80 (Abcam ab6640) at a 1:200 dilution for 1 h at room temperature. This was imaged using an Olympus VS120 microscope at ×20 magnification in the DAPI (nuclei), FITC (autofluorescence), TRITC (F4/80) and Cy5 (nanoparticles) channels. Images were visualized using ImageJ to identify macrophages ($F4/80^+$), hepatocytes (autofluorescence$^+$) and nanoparticles. Macrophages were gated manually on $F4/80^+$ cells and hepatocytes were gated manually on $F4/80^-$autofluorescent$^+$ cells using imageJ. These gates were used as masks to quantify the average Cy5 nanoparticle intensity per cell.

3D microscopy. *Labelling preparation.* Samples were prepared for and imaged via 3D microscopy as previously described[36,60]. Mice were injected with GSL-1-Cy3 (150 µg, Vector Labs, conjugated with 15 µg Cy3-NHS, click chemistry tools) 5 min before euthanization to label blood vessels.

Perfusion fixation. Mice were perfusion-fixed using 60 ml saline solution (PBS 0.5% (w/v) sodium nitrite, 10 U ml^{-1} Heparin) and 80 ml monomer fixative solution (PBS 2% (w/v) acrylamide, 4% (v/v) formaldehyde, 0.25% VA-044 initiator). Tissues were fixed for 7 days in monomer solution, then degassed, purged with argon and incubated at 37 °C for 3 h to polymerize the acrylamide and convert the tissue into a hydrogel. Tissue blocks of 1 mm thickness were placed in clearing solution (4% (w/v) sodium dodecyl sulfate, 200 mM sodium borate, pH 8.5) for 10 days, transferred to borate solution (200 mM sodium borate, pH 8.5, 0.1% (w/v) TritonX-100, 0.01% (w/v) sodium azide) for 1 day, stained with DAPI (400 pmol per mg of tissue) for 2 days, transferred back to a borate solution for 1 day and then placed in a TDE solution (67% 2,2'-thiodiethanol, 33% borate solution) for 1 day before imaging.

Imaging. Tissue blocks were imaged on a Zeiss Lightsheet Z.1 microscope using a ×20, NA 1.0, refractive index (RI) 1.45 clearing objective. Images were acquired at ×0.7 zoom. Gold nanoparticles were visualized using dark-field imaging on the same microscope by removing the laser block and emission filters[36]. Three stacks were acquired for each sample.

Image analysis. Images were imported into MATLAB using the Bio-Formats toolbox and downsampled in the x and y directions to achieve isotropic resolution in all dimensions. Blood vessels (GSL-1-Cy3) were segmented using ilastik[61] and distances from the blood vessels were assessed using a Euclidean distance transformation. Nanoparticle intensity (dark-field scattering intensity) was normalized to the maximum intensity at the blood vessel wall in a given image. Normalized mean nanoparticle intensity was plotted as a function of distance from the nearest blood vessel. All code for the analysis can be found on GitHub at https://github.com/BenKingston/nanoparticle_vessel_analysis.

Tumour disaggregation for single cell analysis. Tumours were collected and stored at 4 °C in PBS until all tumours were dissected from mice. Tumours were manually diced with a razor blade into ≤1 mm^3 pieces. This slurry was transferred into 5 ml of a digestion solution containing Hanks Balanced Salt Solution (HBSS; Gibco 14185052) with 400 μg ml^{-1} collagenase IV (Sigma C5138) and 20 μg ml^{-1} DNase I (Roche 10104159001), pH 7.4, and incubated for 45–60 min under gentle rotation at 37 °C. Disaggregated cells were filtered through a 70 μm mesh strainer, then centrifuged at 500*g* for 5 min. The supernatant was discarded, then the pellet was resuspended in 2 ml of RBC lysis buffer (BioLegend 420301) and incubated for 5 min. Then 13 ml of HBSS was added to the samples, and the sample was centrifuged at 500*g* for 5 min. The supernatant was discarded, and the samples resuspended in 300 μl of blocking buffer containing HBSS, 0.5% (w/v) bovine serum albumin and 2 mM EDTA (BioShop EDT001). Samples were diluted to 25 million cells per ml according to a standardized counter (Beckman Coulter ViCell XR using 'default' cell type) and kept on ice.

Flow cytometry. Stock antibodies were diluted to 1:16 according to our antibody titration experiments (data not shown). All antibodies were purchased from BioLegend: anti-CD45-BV605 (clone 30-F11), anti-CD11b-BV711 (clone M1/70), anti-F4/80-AF488 (clone BM8), anti-Ly6G-PE/Cy7 (clone 1A8), anti-Ly6C-PerCP (clone HK1.4), anti-EpCAM-PE (clone G8.8) and anti-CD31-BV421 (clone 390). Live/dead staining was performed with Zombie NIR (BioLegend 423106) according to the manufacturer's instructions. Antibodies were prepared in a v-bottom 96-well plate (Greiner M8185). FcγR blocking was done using anti-CD16/32 (BioLegend 101302) at a 1:1 dilution for 15 min on ice. Antibody staining was done for 30 min on ice. Two wash steps were performed at 500*g* for 5 min using 200 μl of supernatant. Cells were fixed with 1.6% paraformaldehyde (Thermo Scientific 28906) in HBSS for 30 min, then washed once and stored for up to 5 days at 4 °C before flow cytometry analysis. Events were acquired with a BD LSRFortessa X-20 (BD BioSciences). Gating was based on fluorescence-minus-one (FMO) controls. Compensation was performed using singly stained OneComp beads (eBioscience 01-1111-42), ArC Amine Reactive Compensation beads (Invitrogen A-10346) and RAW264.7 cells with and without Cy5-tagged nanoparticles. Data were analysed using FlowJo 10.0.7 (TreeStar Inc.)[62].

Caelyx-like delivery enhancer liposomes. Empty liposome vehicles were made with similar composition to Caelyx using an extrusion method: 95.8 mg of hydrogenated soy phosphatidylcholine (HSPC) (Avanti Polar Lipids 840058), 32.1 mg of cholesterol (Avanti Polar Lipids 700000) and 32.1 mg of distearoylphosphatidylethanolamine with 2 kDa polyethylene glycol (DSPE-PEG2000) (Avanti Polar Lipids 880128) were dissolved and mixed in 500 μl chloroform (56.4:38.3:5.3 molar ratio). Chloroform was evaporated using a rotary evaporator with 40 °C water bath for 1 h to create a thin lipid film. The lipid film was lyophilized for at least an hour to remove any remaining chloroform. The dried lipid was hydrated with 1 ml PBS to a final lipid concentration of 160 mg ml^{-1}. The lipid mixture underwent five freeze–thaw cycles in liquid nitrogen and a 60 °C water bath, and was then extruded manually 21 times at 60 °C through a 100 nm polycarbonate filter (Whatman WHA800309). Liposomes were characterized by dynamic light scattering and TEM.

Tumour growth and survival. Mice were shaved and inoculated with 4T1 as described above. Tumours were measured using digital calipers three times a week. Mice were injected with delivery enhancer liposomes only, Caelyx (Janssen) only, Caelyx + delivery enhancers or a 5% dextrose control one week after being injected with tumour cells. Volumes were calculated using $V = \text{width}^2 \times \text{length}$. Survival was defined as in the animal protocol; mice were euthanized on meeting protocol endpoints.

Statistics. Statistical analysis was performed using GraphPad Prism 8[63]. Multiple linear regression for the meta-analysis was conducted with SPSS Statistics (v21.0.0.0). Each figure caption describes the statistical test used and the statistical significance convention. Two-tailed unpaired *t*-tests were used to compare the means of two independent samples against each other. Two-way ANOVA was used to compare the influence of two independent variables on a continuous dependent variable, and determine whether the two independent variables have synergistic interactions. The Bonferroni adjustment corrects for multiple post-hoc analyses, as more tests result in more chances a type I error would be made. We chose Bonferroni because it is the most stringent adjustment ($P = \alpha/n$, where $\alpha = 0.05$ and n is the number of post-hoc tests used) and therefore maximizes the robustness of conclusions from our results. All groups in *t*-tests and ANOVAs were assumed to be normally distributed and with equal standard deviation between groups. Statistical significance was determined when $P < \alpha$, where $\alpha = 0.05$.

Reporting Summary. Further information on research design is available in the Nature Research Reporting Summary linked to this article.

Data availability

The data that support the findings of this study are available within the paper and its Supplementary Information files. The raw data that support the findings of this study are available from the corresponding author on reasonable request. Additional data from the meta-analysis of literature are available from the Cancer Nanomedicine Repository at http://inbs.med.utoronto.ca/cnr/.

Code availability

All code (used to run the simulation data in Supplementary Figs. 12 and 13) is available via GitHub at https://github.com/beeno/trillionParticlesODEs. All code for 3D image analysis is available via GitHub at https://github.com/BenKingston/nanoparticle_vessel_analysis.

References

54. Jensen, A. I. et al. Remote-loading of liposomes with manganese-52 and in vivo evaluation of the stabilities of 52Mn-DOTA and 64Cu-DOTA using radiolabelled liposomes and PET imaging. *J. Control. Release* **269**, 100–109 (2018).
55. Pulaski, B. A. & Ostrand-Rosenberg, S. Mouse 4T1 breast tumor model. *Curr. Protoc. Immunol.* **39**, 20.2.1–20.2.16 (2000).
56. Albanese, A., Tsoi, K. M. & Chan, W. C. W. Simultaneous quantification of cells and nanomaterials by inductive-coupled plasma techniques. *J. Lab. Autom.* **18**, 99–104 (2013).
57. Schindelin, J. et al. Fiji: an open-source platform for biological-image analysis. *Nat. Methods* **9**, 676–682 (2012).
58. Adobe Photoshop 21.0.2 (Adobe, 2019).
59. Akima, H. A New Method of interpolation and smooth curve fitting based on local procedures. *J. ACM* **17**, 589–602 (1970).
60. Sindhwani, S. et al. Three-dimensional optical mapping of nanoparticle distribution in intact tissues. *ACS Nano* **10**, 5468–5478 (2016).
61. Berg, S. et al. ilastik: interactive machine learning for (bio)image analysis. *Nat. Methods* **16**, 1226–1232 (2019).
62. FlowJo Software v.10.0.7 (Becton, Dickinson and Company, 2019).
63. GraphPad Prism v.8.4.0 (GraphPad Software).

Acknowledgements

We thank W. Jiang, W. Hou and T. Komal for help with experiments involving radioactivity, S. Lheureux for Caelyx and M. Ganguly, V. Bradaschia and K. Duffin in Pathology at The Centre for Phenogenomics for histology and blood biochemistry. We thank M. Egeblad for the c-fms-EGFP BALB/c breeder mice, and S. Grinstein for RAW264.7 cells. We thank L. Dunning and the Division of Comparative Medicine for animal husbandry. We thank J. Rothschild, C. E. Shin, S. Wilhelm, S. MacParland, J. Jonkman, S. Grinstein and K. Kataoka for discussions. We thank A. Malekjahani, B. Udugama, S. MacParland, M. Rajora, J. Ngai and S. Wilhelm for discussions with the manuscript revisions. We thank the Toronto Nanomedicine Fabrication Centre for use of the ICP-MS, the Nanoscale Biomedical Imaging Facility for use of the TEM and the Advanced Optical Microscopy Facility for guidance and use of the intravital microscope. This work was supported by the Canadian Cancer Society (grant numbers 502200 and 706286), the Canadian Institutes of Health Research (grant numbers PJT-148848 and FDN-159932), the Natural Sciences and Engineering Research Council of Canada (grant number 2015–06397), the Canada Research Chair Program (grant numbers 950–223924 and 950–232468), the Canada Foundation for Innovation (grant number 21765) and the Princess Margaret Cancer Foundation. B.O. thanks the Vanier Canada Graduate Scholarship, CIHR and the McLaughlin Centre for MD/PhD studentships, and the Ontario Graduate Scholarships, the Institute of Biomaterials and Biomedical Engineering, the University of Toronto School of Graduate Studies, the Donnelly Centre, the Frank Fletcher Memorial Fund, C. Yip and J. J. Ruffo for graduate fellowships. W.P. thanks the CIHR and OGS for graduate scholarships, and acknowledges fellowship support from C. Yip, B. and F. Milligan and the University of Toronto Faculty of Applied Science and Engineering. Y.-N.Z. thanks the NSERC, Wildcat Foundation, Ontario Graduate Scholarship, and Paul and Sally Wang fellowships. B.R.K. thanks NSERC, the Donnelly Centre, the Wildcat Fellows Program, the Royal Bank of Canada and Borealis AI for student fellowships and scholarships. A.J.T. thanks CIHR for the provision of a postdoctoral fellowship. M.S.V. thanks the Department of Defense Ovarian Cancer Research Program and the Terry Fox Research Institute for funding. J.C.-S. thanks the University of Toronto Faculty of Medicine for funding. P.M. thanks the Walter C. Sumner foundation for the fellowship.

Author contributions

B.O., W.P., Y.-N.Z. and W.C.W.C. conceptualized the project. B.O., W.P., Y.-N.Z., Z.P.L., B.R.K., A.M.S., A.J.T., P.M. and J.C.-S. designed and performed the nanoparticle synthesis and biodistribution experiments. J.C., M.S.V. and B.O. designed and performed the radioactive liposome validation biodistribution experiments. B.O., W.P., Y.-N.Z. and Z.P.L. designed and performed the delivery enhancer experiments. B.R.K., A.M.S. and P.M. designed and performed the 3D tissue microscopy experiments. Y.Z. designed and performed the protein corona analysis experiments. G.Z. and W.C.W.C. acquired funding for this project. B.O. and W.C.W.C. wrote the initial manuscript draft. All authors contributed to reviewing and editing the manuscript.

Competing interests

B.O., W.P., Y.-N.Z., Z.P.L. and W.C.W.C. declare patents pending on the delivery enhancer technique in the United States (63/017,322) and Canada (3,079,765).

Additional information

Supplementary information is available for this paper at https://doi.org/10.1038/s41563-020-0755-z.

Correspondence and requests for materials should be addressed to W.C.W.C.

Reprints and permissions information is available at www.nature.com/reprints.

nature research

Corresponding author(s): Warren Chan

Last updated by author(s): Jun 12, 2020

Reporting Summary

Nature Research wishes to improve the reproducibility of the work that we publish. This form provides structure for consistency and transparency in reporting. For further information on Nature Research policies, see Authors & Referees and the Editorial Policy Checklist.

Statistics

For all statistical analyses, confirm that the following items are present in the figure legend, table legend, main text, or Methods section.

n/a	Confirmed	
☐	☒	The exact sample size (*n*) for each experimental group/condition, given as a discrete number and unit of measurement
☐	☒	A statement on whether measurements were taken from distinct samples or whether the same sample was measured repeatedly
☐	☒	The statistical test(s) used AND whether they are one- or two-sided *Only common tests should be described solely by name; describe more complex techniques in the Methods section.*
☒	☐	A description of all covariates tested
☐	☒	A description of any assumptions or corrections, such as tests of normality and adjustment for multiple comparisons
☐	☒	A full description of the statistical parameters including central tendency (e.g. means) or other basic estimates (e.g. regression coefficient) AND variation (e.g. standard deviation) or associated estimates of uncertainty (e.g. confidence intervals)
☐	☒	For null hypothesis testing, the test statistic (e.g. *F*, *t*, *r*) with confidence intervals, effect sizes, degrees of freedom and *P* value noted *Give P values as exact values whenever suitable.*
☒	☐	For Bayesian analysis, information on the choice of priors and Markov chain Monte Carlo settings
☒	☐	For hierarchical and complex designs, identification of the appropriate level for tests and full reporting of outcomes
☐	☒	Estimates of effect sizes (e.g. Cohen's *d*, Pearson's *r*), indicating how they were calculated

Our web collection on statistics for biologists contains articles on many of the points above.

Software and code

Policy information about availability of computer code

Data collection	No software was used for data collection.
Data analysis	MATLAB 2019b was used to simulate the compartment model of nanoparticle transport. (MATLAB code is available at the links https://github.com/beeno/trillionParticlesODEs for modelling, and https://github.com/BenKingston/nanoparticle_vessel_analysis for 3D image analysis.) Ilastik was used for image segmentation. GraphPad Prism 8 was used for statistical analysis. SPSS 21.0.0.0 was used for multivariable statistical analysis. FlowJo 10.0.7 was used for flow cytometry analysis. ImageJ/FIJI7 version 2.0.0-rc-69/1.52p was used for image quantification. Scaffold was used for protein corona mass spectrometry analysis. Adobe Photoshop 2020 was used for image editing. Adobe Illustrator 2020 was used for making figures.

For manuscripts utilizing custom algorithms or software that are central to the research but not yet described in published literature, software must be made available to editors/reviewers. We strongly encourage code deposition in a community repository (e.g. GitHub). See the Nature Research guidelines for submitting code & software for further information.

Data

Policy information about availability of data

All manuscripts must include a data availability statement. This statement should provide the following information, where applicable:

- Accession codes, unique identifiers, or web links for publicly available datasets
- A list of figures that have associated raw data
- A description of any restrictions on data availability

The authors declare that the data supporting the findings of this study are available within the paper and its supplementary information files. The raw data supporting the findings of this study are available from the corresponding author upon reasonable request. Additional data from the meta-analysis of literature is available from the Cancer Nanomedicine Repository: http://inbs.med.utoronto.ca/cnr/

Field-specific reporting

Please select the one below that is the best fit for your research. If you are not sure, read the appropriate sections before making your selection.

☒ Life sciences ☐ Behavioural & social sciences ☐ Ecological, evolutionary & environmental sciences

For a reference copy of the document with all sections, see nature.com/documents/nr-reporting-summary-flat.pdf

Life sciences study design

All studies must disclose on these points even when the disclosure is negative.

Sample size	We analyzed samples using at least 3 mice to determine statistical similarity or difference between groups. For the therapeutic efficacy experiments, we performed a power analysis to determine the sample size to study: According to a 2014 study (Kohli AG, Journal of Controlled Release, 2014), 1) 4T1 tumours in BALC/c mice grew to roughly 1700 ±250 mm3 by 37 days with control PBS injection (note, our endpoint will be at 1500 mm3, and we use this number as reference to other studies), and with 2) Doxil injection at Day 15, are reduced to 1100±300 mm3. Our study requires two groups. 1) 0.1x Doxil: estimated to slightly reduce growth to 1600±300 mm3 2) 0.2x Doxil + 9x empty liposomes: estimated to reduce growth to 1100±300 mm3 Using these parameters with an ANOVA repeated measures, between-factors test, and loosening the standard deviation constraint to 400 mm3, we determined the effect size f = 0.81 requires a total sample size of n = 36 (6 per group). To ensure an effect in case of poor tumour growth or unexpected animal euthanasia due to early metastatic burden, we rounded to 7 mice per group. All mice grew as expected and were included in the study and analysis. In the co-injection versus sequential injection experiments, we estimated a smaller difference between groups and rounded to 9 mice per group. For all other experiments, no calculations were done and a sample size was chosen to have minimum n = 3 for statistics. For the chronic toxicity studies at 1.4 years after injection, there were only 2 animals that survived their treatments to be analyzed (no statistical calculations were performed).
Data exclusions	For the MMTV-PyMT studies in Supplementary Figure 9b, 1 liver and 1 tumour was excluded from the analysis, as the samples were broken during preparation. Because the remaining sample sizes were still large enough, we did not repeat these samples, as it was unlikely to change the conclusion of those experiments. For the meta-analysis, reports were excluded if we could not reasonably re-calculate a dose in number of nanoparticles using descriptions from the materials and methods and results sections. A list of reasons why each report was excluded is given in Supplementary Table 2.
Replication	This dose threshold concept and selected experiments have been reproduced for projects independent to this paper by 1) other members of our lab and 2) members of an external lab. The dose threshold has been replicated within this paper using different systems investigating the same concept. Specific examples include: the high vs low dose phenomenon was repeated in 3 sizes of gold nanoparticles, 4 different types of nanoparticles, and 5 mouse tumour models, using a variety of conventional nanoparticle quantification techniques including ICP-MS, fluorescence, and radioactive labelling. All attempts to assess the repeatability of this dose phenomenon were successful in each of these situations, demonstrating reproducibility and robustness. The materials and methods section has been written in as much detail as possible to maximize reproducibility by readers.
Randomization	For tumour growth experiments, the mice were assigned to equal growth groups at day 7 just before injection of nanoparticles to ensure equal growth rates between groups before treatment. For all other experiments, mice were randomly assigned to each experimental group in all experiments because we did not expect any specific confounding variables.
Blinding	Tumour measurements were performed mainly by 1 researcher and occasionally by 2 other researchers to check inter-person measurement variability (there was minimal). These researchers were blinded to the treatment. Intravital microscopy experiments were not blinded and were performed by 1 researcher because of the technical difficulty of the technique. For all other experiments, there was no blinding because the measurements were quantified by assays that eliminated subjective interpretation.

Reporting for specific materials, systems and methods

We require information from authors about some types of materials, experimental systems and methods used in many studies. Here, indicate whether each material, system or method listed is relevant to your study. If you are not sure if a list item applies to your research, read the appropriate section before selecting a response.

Materials & experimental systems

n/a	Involved in the study
☐	☒ Antibodies
☐	☒ Eukaryotic cell lines
☒	☐ Palaeontology
☐	☒ Animals and other organisms
☒	☐ Human research participants
☒	☐ Clinical data

Methods

n/a	Involved in the study
☒	☐ ChIP-seq
☐	☒ Flow cytometry
☒	☐ MRI-based neuroimaging

Antibodies

Antibodies used

All flow cytometry antibodies were purchased from BioLegend: anti-CD45-BV605 (clone 30-F11; cat #103139), anti-CD11b-BV711 (clone M1/70, cat #101241), anti-F4/80-AF488 (clone BM8, cat #123120), anti-Ly6G-PE/Cy7 (clone 1A8, cat #127618), anti-Ly6C-PerCP (clone HK1.4, cat #128028), anti-EpCAM-PE (clone G8.8, cat #118206), anti-CD31-BV421 (clone 390, cat #102423). Live/Dead staining was performed with Zombie NIR (BioLegend 423106).

Immunohistochemistry staining antibodies included: anti-F4/80 (Abcam ab6640), Armenian Hamster Anti-CD209b (ThermoFisher Scientific 14-2093-81), Goat Anti-Armenian Hamster Alexafluor 488 (Abcam ab173003).

Specific dilutions are listed in the Materials and Methods of the Supplementary Info.

Validation

Flow cytometry antibody validations:
anti-CD45-BV605 (clone 30-F11; cat #103139): We validated our results against example plots by the manufacturer (BioLegend): "C57BL/6 mouse splenocytes were stained with CD45 (clone 30-F11) Brilliant Violet 605™ (filled histogram) or rat IgG2b, κ Brilliant Violet 605™ isotype control (open histogram)." BioLegend validation for mouse cells in flow cytometry: "Each lot of this antibody is quality control tested by immunofluorescent staining with flow cytometric analysis."

anti-CD11b-BV711 (clone M1/70, cat #101241): We validated our results against example plots by the manufacturer (BioLegend): "C57BL/6 mouse bone marrow cells were stained with CD11b (clone M1/70) Brilliant Violet 711™. Data shown was gated on the myeloid cell population." BioLegend validation for mouse cells in flow cytometry: "Each lot of this antibody is quality control tested by immunofluorescent staining with flow cytometric analysis."

anti-F4/80-AF488 (clone BM8, cat #123120): We validated our results against example plots by the manufacturer (BioLegend): "Thioglycolate-elicited Balb/c mouse peritoneal macrophages stained with BM8 Alexa Fluor® 488." BioLegend validation for mouse cells in flow cytometry: "Each lot of this antibody is quality control tested by immunofluorescent staining with flow cytometric analysis."

anti-Ly6G-PE/Cy7 (clone 1A8, cat #127618): We validated our results against example plots by the manufacturer (BioLegend): "C57BL/6 bone marrow cells stained with 1A8 PE/Cyanine7" BioLegend validation for mouse cells in flow cytometry: "Each lot of this antibody is quality control tested by immunofluorescent staining with flow cytometric analysis."

anti-Ly6C-PerCP (clone HK1.4, cat #128028): We validated our results against example plots by the manufacturer (BioLegend): "C57BL/6 bone marrow cells were stained with Ly-6C (clone HK1.4) PerCP. Data shown was gated on myeloid cell population." BioLegend validation for mouse cells in flow cytometry: "Each lot of this antibody is quality control tested by immunofluorescent staining with flow cytometric analysis."

anti-EpCAM-PE (clone G8.8, cat #118206): We validated our results against example plots by the manufacturer (BioLegend): "TE-71 (mouse thymic epithelial stromal cell line) cells were stained with CD326 (clone G8.8) PE (filled histogram) or rat IgG2a, κ PE isotype control (open histogram)." BioLegend validation for mouse cells in flow cytometry: "Each lot of this antibody is quality control tested by immunofluorescent staining with flow cytometric analysis."

anti-CD31-BV421 (clone 390, cat #102423): We validated our results against example plots by the manufacturer (BioLegend): "Thioglycolate-elicited Balb/c mouse peritoneal macrophages stained with BM8 Alexa Fluor® 488." BioLegend validation for mouse cells in flow cytometry: "Each lot of this antibody is quality control tested by immunofluorescent staining with flow cytometric analysis."

Live/Dead staining was performed with Zombie NIR (BioLegend 423106): We validated our results against example plots by the manufacturer (BioLegend): "One day old C57BL/6 mouse splenocytes were stained with Zombie NIR™ and analyzed before fixation (purple) or after fixation and permeabilization (red). Cells alone, without Zombie NIR™ staining, are indicated in black." We also validated against live and dead in vitro cells, as well as spleens, lymph nodes, tumours, and livers. BioLegend validation for mouse cells in flow cytometry: "Each lot of this antibody is quality control tested by immunofluorescent staining with flow cytometric analysis."

==========
Immunohistochemistry antibody validations:

anti-F4/80 (Abcam ab6640): Validated by Abcam: "This antibody recognises the mouse F4/80 antigen, a 160kD glycoprotein

expressed by murine macrophages ("Abpromise guarantee"). We validated against distribution seen in F4/80 in Tavares, PNAS, 2017.

Armenian Hamster Anti-CD209b (ThermoFisher Scientific 14-2093-81). Validated against CD209b distribution seen in Poon, ACS Nano, 2019 and The Human Protein Atlas https://www.proteinatlas.org/ENSG00000090659-CD209/tissue/liver.

Goat Anti-Armenian Hamster Alexafluor 488 (Abcam ab173003) was used to visualize the distribution of these two antibodies.

Eukaryotic cell lines

Policy information about cell lines

Cell line source(s)	4T1 cells were from ATCC. RAW264.7 cells were from ATCC. MDA-MB-231 cells were from ATCC. U87MG cells were from ATCC.
Authentication	Cell lines were not authenticated. 4T1 cells were validated for EpCAM expression before inducing into mice.
Mycoplasma contamination	4T1 cells tested negative for mycoplasma contamination. Other cell lines were not tested.
Commonly misidentified lines (See ICLAC register)	Cells used were not from commonly misidentified lines.

Animals and other organisms

Policy information about studies involving animals; ARRIVE guidelines recommended for reporting animal research

Laboratory animals	Mice strains used: female BALB/c, nude CD-1, MMTV-PyMT on FVB/n, Csf1r-EGFP on BALB/c. Age:BALB/c were studied between 6-8 weeks of age. CD-1 nude were studied between 10-14 weeks of age. MMTV-PyMT on FVB/n mice were studied between 10-13 weeks of age. Csf1r-EGFP on BALB/c mice were studied between 8-10 weeks of age.
Wild animals	No wild animals were used in this study.
Field-collected samples	No field-collected samples were used in this study.
Ethics oversight	All animal research was reviewed by and conducted in accordance with the animal ethics committee from the Division of Comparative Medicine at the University of Toronto (protocols #20011909, #20012099, #20011605) and the Animal Resources Centre at the Unversity Health Network

Note that full information on the approval of the study protocol must also be provided in the manuscript.

Flow Cytometry

Plots

Confirm that:

☒ The axis labels state the marker and fluorochrome used (e.g. CD4-FITC).

☒ The axis scales are clearly visible. Include numbers along axes only for bottom left plot of group (a 'group' is an analysis of identical markers).

☒ All plots are contour plots with outliers or pseudocolor plots.

☒ A numerical value for number of cells or percentage (with statistics) is provided.

Methodology

Sample preparation	See supplementary information for methods. Tumours were collected and stored in 4°C PBS until all tumours were dissected from mice. Tumours were manually diced with a razor blade into ≤ 1mm^3 pieces. This slurry was transferred into 5 mL of a digestion solution containing Hanks Balanced Salt Solution (HBSS; Gibco 14185052) with 400 µg/mL collagenase IV (Sigma C5138) and 20 µg/mL DNase I (Roche 10104159001), pH 7.4, and incubated for 45-60 minutes under gentle rotation at 37°C. Disaggregated cells were filtered through a 70 µm mesh strainer, then centrifuged at 500 x g for 5 minutes. The supernatant was discarded, then the pellet was resuspended in 2 mL of RBC lysis buffer (BioLegend 420301) and incubated for 5 minutes. 13 mL of HBSS was added to the samples, and the sample was centrifuged at 500 x g for 5 minutes. The supernatant was discarded, and the samples resuspended in 300 µL of blocking buffer containing HBSS, 0.5% (w/v) bovine serum albumin, and 2 mM EDTA (BioShop EDT001). Samples were diluted to 25 million cells / mL according to a standardized counter (Beckman Coulter ViCell XR using "default" cell type) and kept on ice. Liver perfusion and disaggregation for single cell analysis: The mouse was anesthetized using isoflurane (5% induction, 2% maintenance). A horizontal skin incision was made across the abdomen midline. Skin was retracted and the same incision was made onto the peritoneum to expose the viscera. Intestines were gently displaced outside to the left of the mouse to expose the portal vein and vena cava. A 21G needle connected to a

peristaltic pump was inserted into the portal vein, the vena cava was cut open (to allow outflow), and perfusion was performed for 5 minutes at 5 mL/minute with a 10 U/mL heparin solution in 1x PBS (calcium-free). The liver was observed to turn in colour from red to brown. The solution was then exchanged for 3 mg/mL collagenase in HBSS at a flow rate of 5 mL/minute for 5 minutes to digest. The liver was observed to turn in colour from brown to tan/yellow. When the colour change was patchy, it indicated suboptimal perfusion; in these cases the 21G was poked into the liver and flow rate was reduced. At the end of digestion, the liver was carefully excised and placed into a solution of HBSS. The Glisson's capsule was cut and the liver was gently agitated with tweezers to dissociate hepatic cells into the solution. This cell solution was centrifuged at 25g for 2 minutes. The supernatant was labelled as non-parenchymal cells and the pellet was labelled as parenchymal cells. A portion of parenchymal cells were visualized under DIC microscopy to assess presence of hepatocytes; if no hepatocytes, we deemed the perfusion/digestion a failure and discarded the sample. Samples were diluted to 25 million cells / mL according to a standardized counter (Beckman Coulter ViCell XR using "default" cell type) and kept on ice.

Instrument	BD LSRFortessa X-20 (BD BioSciences)
Software	Data were analyzed using FlowJo 10.0.7 (TreeStar Inc.)
Cell population abundance	We collected at least 30,000 live cells for quantifying the amount of cells that took up nanoparticles.
Gating strategy	Gating strategies are described with the figures wherever flow cytometry is reported. Briefly, all analysis began with FSC vs SSC plots, and small debris (FSC low and SSC low) were gated out by eye. Next, FSC-A vs FSC-H plots were used and all cells that aligned on the major slope were gated in. If there were two slopes, the halfway slope was used as the cutoff between positive and negative populations. Further gating was performed in an experiment-specific manner (see manuscript details). Nanoparticle-positive gates were defined as the 99% region above a nanoparticle-free control.

☒ Tick this box to confirm that a figure exemplifying the gating strategy is provided in the Supplementary Information.